


Application of response surface methodology and computational fluid dynamics for analyzing and optimizing the performance of finned solar air heater

Proc IMechE Part C:
J Mechanical Engineering Science
1–30
© IMechE 2024
Article reuse guidelines:
sagepub.com/journals-permissions
DOI: 10.1177/09544062241278187
journals.sagepub.com/home/pic


Vineet Singh 

Abstract

In this research paper, a Solar Air Heater (SAH) with triangular fins has been experimentally and numerically analyzed and validated. The novelty of this work is the selection of the type of the fins, the triangular fins not only enhance the turbulence and heat transfer to the air but have lower material consumption as compared to the rectangular fins. The ANSYS 2022, Computational Fluid Dynamics (CFD) software has been used for the numerical study, the post processor simulation results of the velocity, pressure, and temperature field at velocity, pressure and Roserland boundary conditions has been determined by using $k-\epsilon$ standard turbulence model at steady state. The heat transfer coefficient and friction factor are two important parameters that are used for determining the heat transfer rate and pressure drop over the surface of the Solar Air Heater (SAH). For enhancing the heat transfer rate and minimizing the pressure drop, a optimized geometry of the fins must be required. In consideration of this fact, in this research, the Heat transfer Coefficient (HTC) and Friction factor (FF) have been optimized by the Response Surface Methodology (RSM). The two important input variables namely Reynolds Number (Re) and pitch to height ratio (p/L) of the fins has been selected for maximizing the performance of the SAH. The simulation results of the velocity contour shows that the velocity reached maximum between the narrow gap of the triangular fins due to conservation of mass. So, velocity of the flowing air increasing in between the fins. The optimum values of response parameters namely Nusselt Number, friction factor and Thermal Performance Factor are obtained to be 176.5064, 0.0260, and 1.8903 at Reynolds Number 16928.2180 and P/L 1.3430.

Keywords

Solar air heater, CFD, fins, exergy, RSM, Air

Date received: 28 September 2023; accepted: 29 June 2024

Introduction

Solar energy is a green energy source due to its pollution-free nature which is used in a number of applications. One application of solar energy is for heating the air is very popular. The heated air can be used for a number of applications like drying the crops, wood and heating the room.¹ In the Solar Air Heater (SAH) cold air flow over the black painted absorber plate. The absorber plate is made by the high thermal conductive material like copper, aluminum and galvanized iron sheet of 1–2 mm thickness.² A transparent glass cover have been fixed over the SAH for reducing the thermal losses. For increasing the heat transfer capacity of the SAH, the absorber plate have been provided with various projections like v cut tap twisted turbulator,³ inclined vortex plate,⁴ S

shaped ribs,⁵ quarter circular ribs,⁶ hybrid ribs,⁷ and many more design. The roughness on the absorber plate increases the turbulence and heat transfer from the absorber plate to the air. Based on the flow pattern of the air, glazing, application, storage material, type of the absorber plate roughness, and available energy source, the solar air heater has been classified.

Department of Mechanical Engineering, School of Engineering & Technology, IFTM University, Moradabad, Uttar Pradesh, India

Corresponding author:

Vineet Singh, Department of Mechanical Engineering, School of Engineering & Technology, IFTM University, Moradabad, E-4 Sanjay Nagar, Government Hospital Ghaziabad, Bareilly, Uttar Pradesh 243006, India.

Email: vineetpsh@gmail.com

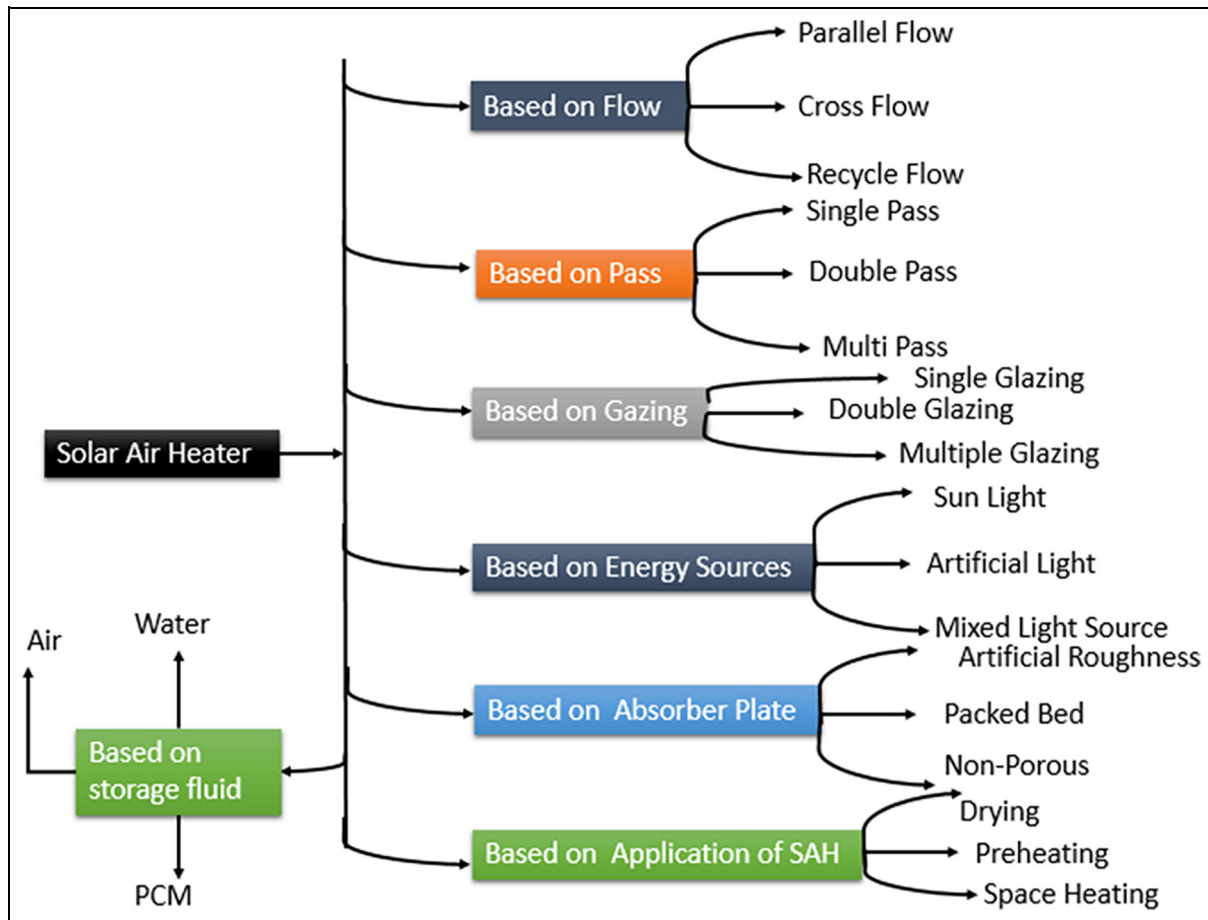


Figure 1. Various types of the SAH.

The pictorial view of the classification of the solar air heater is representing in the Figure 1.

The roughened absorber plate increased the heat transfer rate but simultaneously enhanced the pressure drop on the absorber plate. The higher pressure drop consumes higher blower power and enhanced losses in exergy⁸ due to that Thermal Performance Factor (TPF) has been reduced. The TPF is the ratio of the increment of Nusselt Number and friction factor over the roughened surface as compared with smooth surface.² The roughened surface enhance turbulence and due to that, the heat transfer rate increased. On the other hands fins not only increased the turbulence but also promotes the heat transfer from absorber plate to the air. The number of the researcher used the various types of the fins on the absorber plate of the SAH. The Table 1 shows the various types of the fins used in previously published research article with their performance parameters.

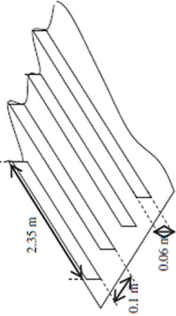
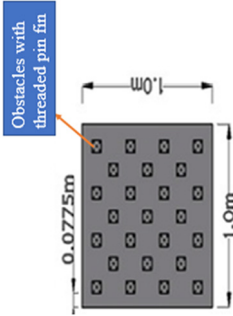
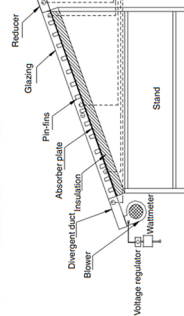
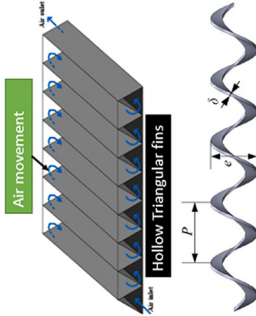
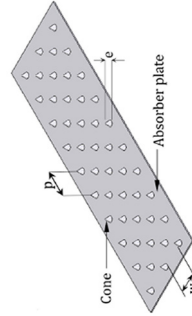
The numerical techniques like Computational Fluid Dynamics (CFD) is very useful tool for analyzing the flow field of the SAH. It shows the temperature, pressure and velocity contour at different locations in day time. Table 2 represents the CFD techniques used by the various resaecher with their performnace parameters like Nusselt Number, Friction Factor and TPF.

The CFD analysis gives the temperature, velocity and pressure field on the absorber plate at various locations. The performance parameters like Nusselt Number, friction factor, heat transfer, thermal efficiency, and exergy efficiency calculated by empirical relations. The Table 3 shows the various empirical relation used for calculation of the Nusselt Number and friction factor on smooth and roughened surfaces. The Nusselt number and friction factor are the two most important parameters which can helps to determine the heat transfer and blower power spent for blowing the air over the absorber plate.

Table 3 represents the basic equations for determining the Nusselt Number and friction factor in laminar and turbulent flow in SAH. These equations used in various roughened geometry of the SAH. The Nusselt Number helps to determine, the heat transfer coefficient and heat transfer rate from absorber plate to the air, the friction factor used for calculating the pressure drop and blower power requirement.⁸

The numerical techniques are very useful for determining the flow field at various boundary condition in a given flow field so that a optimum geometry can be determined at which the system performance is maximum. In various design of solar air heater number of optimization techniques used like³⁶ used the

Table 1. Various types of the fins used on the absorber plate of the SAH.

S. no.	Fin type	Fins design picture	Concluding parameters	Year of publication	Author's details
1	Rectangular fins		The thermal efficiency has been enhanced to be 9% as compared to the without finned surface at mass flow rate 0.09 kg/s.	2013	Fudholi et al. ⁹
2	Obstacles with threaded pin fin		The energy efficiency increased by 23.59% at mass flow rate of 0.0094 kg/s.	2023	Borah et al. ¹⁰
3	Pin fin solar air heater		The outlet temperature enhanced to be 17°C.	2019	Sivakumar et al. ¹¹
4	Triangular fin solar air heater		The maximum thermal performance obtained at 60° angle of the triangular shape fins.	2020	Akhbari et al. ¹²
5	Spiral Fins		Enhanced the heat transfer performance 30.63%–137.1%. The highest THPP is 1.04 for $P_{Dh} = 1.5$ and $N = 5$. The THPP is 0.8233 at $Re = 8000$, $p/e = 10$ and $w/e = 4$.	2024	Du et al. ¹³
6	Cone shaped fins			2022	Alsaiani et al. ¹⁴

(continued)

Table 1. (Continued)

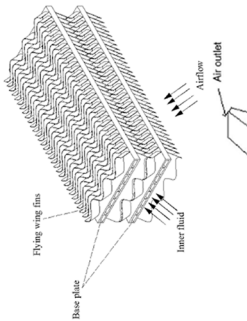
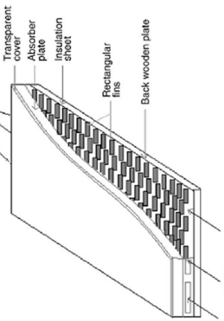
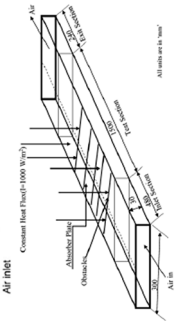
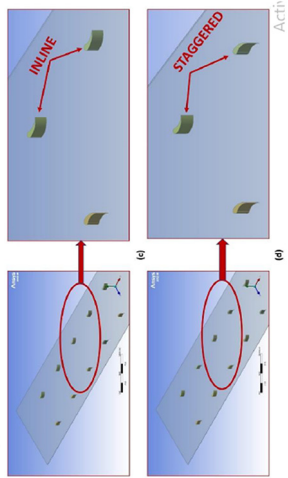
S. no.	Fin type	Fins design picture	Concluding parameters	Year of publication	Author's details
7	Flying wing fins		The tremendous reduction in friction factor has been noted.	2023	Miao et al. ¹⁵
8	Staggered Rectangular Fins		Enhanced the thermal performance from 63% to 80% and simultaneously enhance the pump power from 1.8 to 16 W.	2020	Ammar et al. ¹⁶
9	Rectangular fins			2024	Sharma and Maithani ¹⁷
10	Staggered aerofoil type fins		It enhance the 23.24% thermal efficiency.	2022	Nagaraj et al. ¹⁸

Table 2. CFD analysis on various geometries of the SAH.

S. no.	Geometry of SAH	Numerical technique	Concluding parameters	Year of publication	Author's details
1	Hybrid ribs (Broken arc and Staggered ribs)	CFD	$\frac{Nu_c}{Nu_s} = 3.16$ $\frac{f_c}{f_s} = 2.57$ $TPF = 2.33$	2021	Gill et al. ⁷
2	Circular ribs	CFD	$Nu = 120$ $f = 0.030$	2021	Yadav et al. ¹⁹
3	Trapezoidal ribs	COMSOL	$\frac{Nu_c}{Nu_s} = 5.54$ $\frac{f_c}{f_s} = 36.97$ $TPF = 1.72$	2022	Gogada et al. ²⁰
4	Small diameter transverse wire ribs	CFD	$\frac{Nu_c}{Nu_s} = 1.46$ $\frac{f_c}{f_s} = 2.22$ $TPF = 1.65$	2013	Yadav and Bhagoria ²¹
5	Curved solar air heater	CFD	$\eta_{th} = 91.93\%$	2018	Singh and Singh ²²
6	L shaped ribs	CFD	$TPF = 1.90$	2016	Gawande et al. ²³
7	Cooling fluid channel depth varies	CFD	$d_{optimum} = 10mm$	2010	Sun et al. ²⁴
8	Double pass recycled aluminum tube	COMSOL	$\eta_{th} = 60.2\%$	2019	Al-Damook et al. ²⁵
9	Novel staggered cuboidal baffles	CFD	$TPF = 3.43$	2021	Parsa et al. ²⁶
10	Inclined fins	CFD	$TPF = 1.928$ $\frac{Nu_c}{Nu_s} = 2.53$ $\frac{f_c}{f_s} = 2.22$	2019	Qader et al. ²⁷
11	Arc shape and V shape ribs	CFD	$THPP_V = 2.21$ $THPP_{arcshape} = 1.5$	2020	Srivastava et al. ²⁸

Table 3. Nusselt number and friction factor correlation in various literature.

S. no.	Authors	Year of publication	Nusselt number correlation	Friction factor correlation
1	Garg et al. ²⁹	1991	$Nu = 0.023Re^{0.98}$	$f = 0.059Re^{-0.2}$
2	Karim and Hawlader ³⁰	2006	$Nu = 0.023Re^{0.8} Pr^{0.33}$	-
3	El-Sebaei et al. ³¹	2011	-	For laminar flow $f = \frac{24}{Re}$ For turbulent flow $f = 0.079Re^{-0.25}$
4	Velmurugan and Kalaivanan ³²	2015	$Nu = 0.018Re^{0.8} Pr^{0.4}$	$f = 0.079Re^{-0.25}$
5	Naphon ³³	2005	$Nu = 0.018Re^{0.8} Pr^{0.4}$	-
6	Fudholi et al. ⁹	2013	$Nu = 0.018Re^{0.8} Pr^{0.4}$	For $Re < 2550$ $f = \frac{24}{Re} + 0.9\left(\frac{H}{L}\right)$ For $2550 < Re < 10^4$ $f = 0.0094 + 2.92Re^{-0.15}\left(\frac{H}{L}\right)$
7	Bahrehmand et al. ³⁴	2015	$Nu = 0.018Re^{0.8}$	For laminar flow $f = \frac{64}{Re}$ For turbulent flow $f = 0.079Re^{-0.25}$
8	Priyam and Chand ³⁵	2016	$J = 0.0836Re^{-0.2309}\left(\frac{w}{H_f}\right)^{0.1284}$ $\left(\frac{w}{2.amp}\right)^{-0.153}\left(\frac{L}{\lambda}\right)^{-0.326}$ Where $J = \frac{Nu}{RePr^{\frac{1}{3}}}$	$f = 1.16Re^{-0.309}\left(\frac{w}{H_f}\right)^{0.303}$ $\left(\frac{w}{2.amp}\right)^{-0.25}\left(\frac{L}{\lambda}\right)^{-0.1152}$

Response Surface Methodology (RSM) in the jet plate solar air heater,²⁷ optimized the inclined fins solar air heater by RSM and applied the RSM and ANN on the solar air dryers.

Above literature shows that SAH is the interesting device for heating the air by the solar energy. The Numerical, experimental and optimization studies have been carried by various researcher for improving

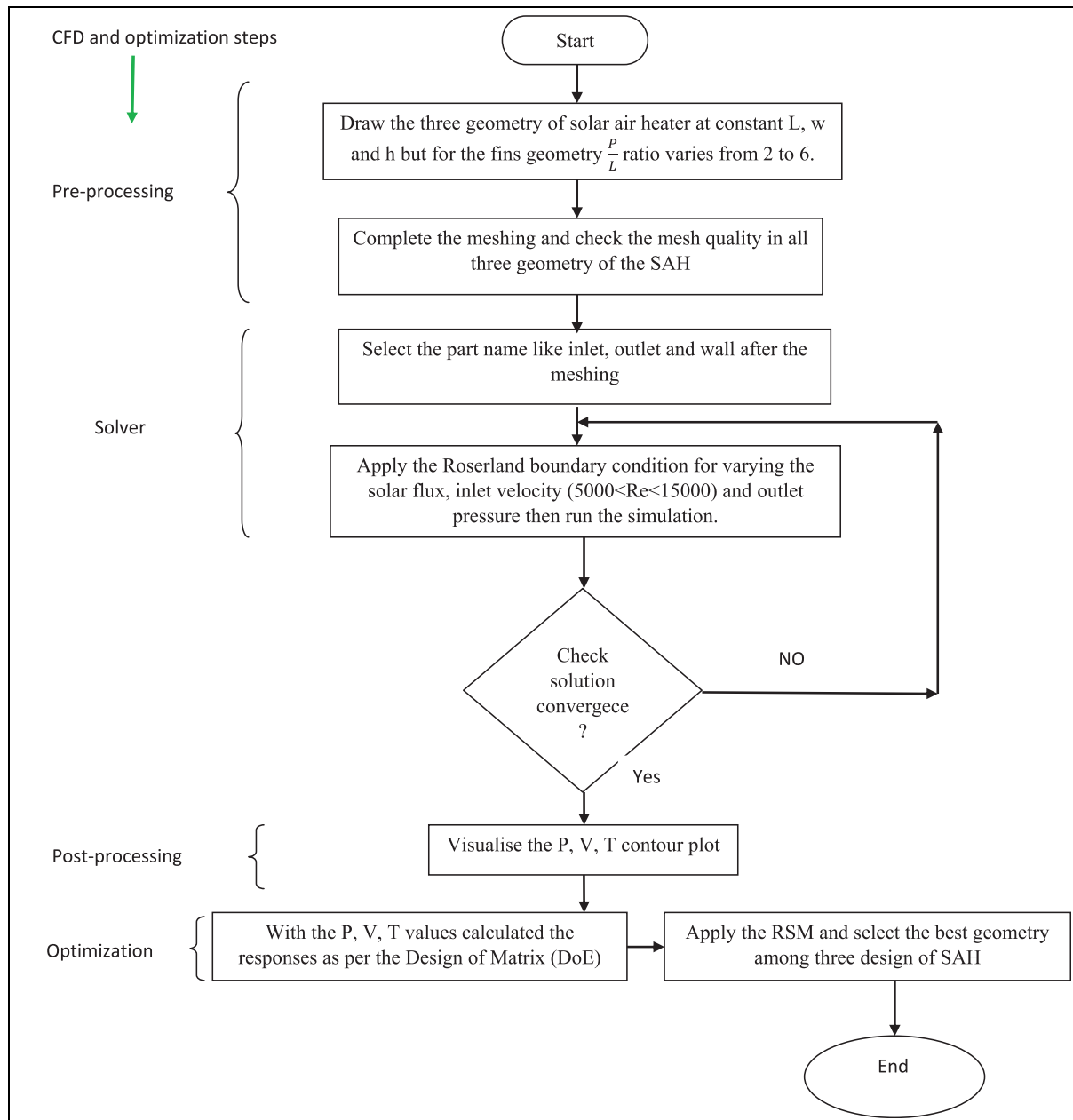


Figure 2. Block diagram of methodology adopted.

the heat transfer characteristics of the solar air heater. The thermal efficiency and thermal hydraulic efficiency represents the energy efficiency of the SAH but the real efficiency has been measured by the exergy efficiency. The Tale 1 represents the various type of the fin design on absorber plate to enhance the turbulence and heat transfer rate. Table 1 clearly shows that with aerofoil fins, conical fins, spiral fins, and rectangular staggered fins enhance the performance parameters like thermal efficiency and THPP, but very few researcher used the triangular fins in staggered manner. Put these thins in mind in this research a staggered triangular fined SAH have been studied by the CFD analysis that is new and novel. Furthermore, the CFD results have been validated with the experimental results and for determining the optimum geometry

of the fins, the system has been optimized by the RSM. The triangular fins are very useful for increasing the turbulence and heat transfer to the air by increasing the surface area of the plate. The system has been optimized to find the optimum value of mass flow rate and the exact geometry of the fins so that performance of SAH is maximum. Because of that the two input variables namely Reynolds Number and fin pitch to height ratio selected for optimizing the system.

Methodology adopted

Figure 2 represents the methodology adopted in the case of design and analysis of the finned solar air heater.

Initially the three geometries of SAH prepared in the ANSYS 2022 at varying pitch to height ratio from 2 to 6. The meshing and the simulation work completed and then the pressure, temperature and velocity field determined and calculated the responses as per the Design of Matrix (DoE). The optimization work has been completed by Response Surface Methodology (RSM) and determine the best geometry which give the best performance. Further, for validating the results, the experimental setup is prepared for best geometry and compared the simulation results with the experimental results.

CFD model equations

Computational Fluid Dynamics (CFD) is a numerical method to solve the fluid and heat transfer problems. It is based on the finite volume approach. In CFD analysis velocity, pressure, and temperature field have been determined with the help of the computer software. The velocity, pressure, and temperature field have been generated by the solution of the continuity, momentum, and energy equation within the boundary conditions. So following are the governing equations at a steady state on which CFD simulation results depend is presented in Ref.⁵

- Conservation of mass equation.

$$\frac{\partial(\rho u)}{\partial x} + \frac{\partial(\rho v)}{\partial y} + \frac{\partial(\rho w)}{\partial z} = 0 \quad (1)$$

- Momentum equation.

- X- Momentum equation

$$\begin{aligned} \rho \left(\frac{u \partial u}{\partial x} + \frac{v \partial u}{\partial y} + \frac{w \partial u}{\partial z} \right) &= \rho g_x - \frac{\partial P}{\partial x} \\ &+ \frac{\partial}{\partial x} \left[2\mu \frac{\partial u}{\partial x} + \lambda \nabla \cdot \vec{V} \right] + \frac{\partial}{\partial y} \left[\mu \left(\frac{\partial u}{\partial y} + \frac{\partial v}{\partial x} \right) \right] \\ &+ \frac{\partial}{\partial z} \left[\mu \left(\frac{\partial u}{\partial z} + \frac{\partial w}{\partial x} \right) \right] \end{aligned} \quad (2)$$

- Y- Momentum equation

$$\begin{aligned} \rho \left(\frac{u \partial v}{\partial x} + \frac{v \partial v}{\partial y} + \frac{w \partial v}{\partial z} \right) &= \rho g_y - \frac{\partial P}{\partial y} \\ &+ \frac{\partial}{\partial x} \left[\mu \left(\frac{\partial v}{\partial x} + \frac{\partial u}{\partial y} \right) \right] + \frac{\partial}{\partial y} \left[2\mu \left(\frac{\partial v}{\partial y} + \lambda \nabla \cdot \vec{V} \right) \right] \\ &+ \frac{\partial}{\partial z} \left[\mu \left(\frac{\partial v}{\partial z} + \frac{\partial w}{\partial y} \right) \right] \end{aligned} \quad (3)$$

- Z- Momentum equation

$$\begin{aligned} \rho \left(\frac{u \partial w}{\partial x} + \frac{v \partial w}{\partial y} + \frac{w \partial w}{\partial z} \right) &= \rho g_z - \frac{\partial P}{\partial z} \\ &+ \frac{\partial}{\partial x} \left[\mu \left(\frac{\partial w}{\partial x} + \frac{\partial u}{\partial z} \right) \right] + \frac{\partial}{\partial y} \left[\mu \left(\frac{\partial v}{\partial z} + \frac{\partial w}{\partial y} \right) \right] \\ &+ \frac{\partial}{\partial z} \left[2\mu \frac{\partial w}{\partial z} + \lambda \nabla \cdot \vec{V} \right] \end{aligned} \quad (4)$$

Energy equation

$$\begin{aligned} \rho C_P \left(\frac{u \partial T}{\partial x} + \frac{v \partial T}{\partial y} + \frac{w \partial T}{\partial z} \right) \\ = \beta T \left(\frac{u \partial P}{\partial x} + \frac{v \partial P}{\partial y} + \frac{w \partial P}{\partial z} \right) + \nabla \cdot (\overline{k \nabla T}) + \phi \end{aligned} \quad (5)$$

Where u , v , and w are the velocity of air in x , y , and z directions and the β is the coefficient of volume expansion. The term ϕ is known as viscous dissipation. It is represented by the following equation.⁴

$$\begin{aligned} \phi &= 2\mu \left[\left(\frac{\partial u}{\partial x} \right)^2 + \left(\frac{\partial v}{\partial y} \right)^2 + \left(\frac{\partial w}{\partial z} \right)^2 \right] \\ &+ \mu \left[\left(\frac{\partial v}{\partial x} + \frac{\partial u}{\partial y} \right)^2 + \left(\frac{\partial v}{\partial z} + \frac{\partial w}{\partial y} \right)^2 + \left(\frac{\partial u}{\partial z} + \frac{\partial w}{\partial x} \right)^2 \right] \\ &+ \lambda \left(\frac{\partial u}{\partial x} + \frac{\partial v}{\partial y} + \frac{\partial w}{\partial z} \right)^2 \end{aligned} \quad (6)$$

Turbulence model

There are several models (Laminar, Inviscid, k-epsilon, k-omega, Transition SST, Reynolds Stress, Scale Adaptive Simulation (SAS), Detached Eddy Simulation (DES), and Large eddy simulation) available, which can be used for determining the flow characteristics in CFD. The selection of the model has been done based on the accuracy of the results. In this SAH model analysis k- ϵ (two equation) model has been used for determining the velocity and pressure distribution with good accuracy.⁴

K- ϵ model. In the k- ϵ model, the k represents the turbulent kinetic energy and ϵ represents the rate of dissipation of turbulence kinetic energy. So two equations are used for representing the total kinetic energy for the turbulent flow. One equation counted the effect of turbulent kinetic energy from total kinetic energy of the turbulent flow. The second equation represents the turbulent kinetic energy due to the dissipation effect of the eddies.

The velocity and length scale is defined in the terms of the k and ϵ by the following equation.²¹

$$v = k^{\frac{1}{2}}, \quad (7)$$

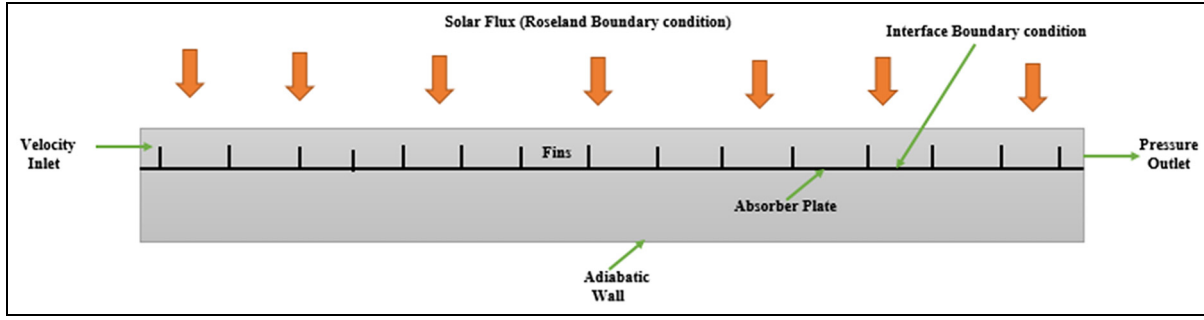


Figure 3. Schematic representation of boundary conditions.

$$l = \frac{k^3}{\varepsilon} \quad (8)$$

$$\Gamma = \frac{1}{3(\alpha + \sigma_S) - C\sigma_S} \quad (13)$$

So following are the two equation representing in the term of k and ε .²¹

$$\frac{\partial(\rho k)}{\partial(t)} + \text{div}(\rho k U) = \text{div} \left[\frac{\mu_t}{\sigma_k} \text{grad} k \right] + 2\mu_t S_{ij} \cdot S_{ij} - \rho \varepsilon \quad (9)$$

$$\begin{aligned} \frac{\partial(\rho \varepsilon)}{\partial(t)} + \text{div}(\rho \varepsilon U) &= \text{div} \left[\frac{\mu_t}{\sigma_\varepsilon} \text{grad} \varepsilon \right] \\ &+ C_{1\varepsilon} \left(\frac{\varepsilon}{k} \right) 2\mu_t S_{ij} \cdot S_{ij} - \frac{C_{2\varepsilon} \rho \varepsilon^2}{k} \end{aligned} \quad (10)$$

Where μ_t represents the eddy viscosity by following equations

$$\mu_t = \frac{\rho C_\mu k^2}{\varepsilon} \quad (11)$$

The value of 5 constants used in the above equation is represented below.²¹

$$\begin{aligned} C_\mu &= 0.09, \sigma_K = 1.00, \sigma_\varepsilon = 1.30, \\ C_{1\varepsilon} &= 1.44 \text{ and } C_{2\varepsilon} = 1.92 \end{aligned}$$

Roseland energy model. The Roseland radiation model is used by the Ansys fluent for calculating the radiation intensity at a particular location at a fixed time at latitude angle. The following equation has been used for defining the radiation intensity presented by the ANSYS FLUENT.³⁷

$$q_r = -\Gamma \nabla G \quad (12)$$

Where q_r is the radiation flux, G is the radiation intensity and Γ is the constant. The Γ is represented by the following equation.³⁷

Where α is the Absorber Coefficients (AC), σ_S is the scattering coefficient and C is the phase function. Now the transport equation solves by the ANSYS FLUENT.³⁸

$$\nabla \cdot (\Gamma \nabla G) - \alpha G + 4an^2 \sigma T^4 = S_G \quad (14)$$

Where n is the refractive index of the medium, σ is the Stefan Boltzmann constant and S_G is the user-defined radiation source.

Boundary conditions

Ansys Fluent 2022 R₂ is used to analyze the SAH with triangular fins on the copper plate AP. The Figure 3 represents the boundary conditions applied on the SAH. So the whole system has been divided into two zones. One is the solid zone for the copper AP and second is the fluid zone represents the air control volume. At the boundary of the solid and fluid zone, there is an interference boundary conditions. At the interference, no-slip boundary conditions are validated as per the k - ε model which depends on the Reynolds number.³⁹

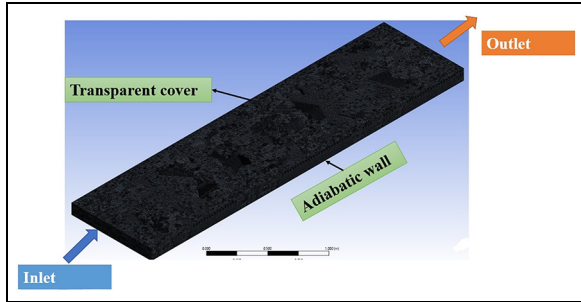
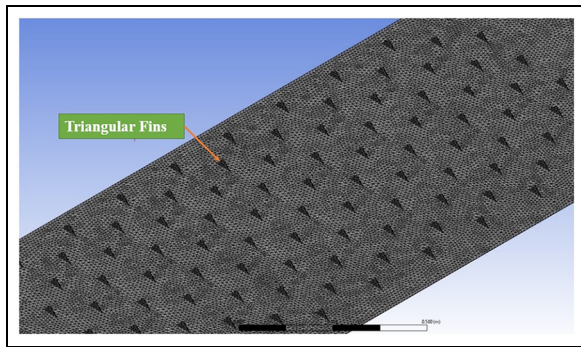
At the inlet of the SAH velocity inlet and at the outlet pressure boundary conditions are applied. The side walls and bottom of the SAH considered as the adiabatic wall. The reading has been collected based on the day and month of the year for which solar ray tracing model is available. The air and the copper material have been selected for the fluid and solid domain. Table 4 represents the properties of copper and the air.

Meshing on the absorber plate and the fluid domain with grid independent test

The CFD results depend on the mesh quality and the element size. In this solar air heater modeling, the total number of triangular surface meshes is 1,750,623

Table 4. Material properties of the air and the copper.²²

Material	Density (kg/m ³)	Specific heat (Kj/kg.K)	Viscosity (kg-m/sec)	Thermal conductivity (W/mK)
Air	1.225	1.006	0.000017894	0.0242
Copper	8978	0.381	-	387.6

**Figure 4.** Mesh on the fluid domain.**Figure 5.** Mesh on the absorber plate.

with the total number of nodes 371,878. The target skewness and pinch tolerance of the mesh is 0.4 and 0.00009 m. the skewness is vary from 0 to 1. The 0 represents the best quality of the mesh and the 1 represents the worst quality of the mesh.⁴⁰ The skewness represents the deviation of real mesh element volume to ideal triangular/ tetrahedral mesh element volume. The element size is selected to be 0.1 mm as shown in Figures 4 and 5. The second parameter of measuring the mesh quality is orthogonality. The minimum value of orthogonality is 0.13 and the maximum value is 0.98. The 0 orthogonality represents the worst quality of mesh and 1 represents the perfect quality of the mesh.

To stabilize the size and accuracy of the mesh grid independent test has been performed. The grid independent test performed in between the mesh number of 4.375×10^5 – 2.51×10^6 at Reynolds Number 10,000 and pitch to height ratio 4. The effect of change of the number of the mesh on percentage variation on Nusselt Number has been presented in the Table 5.

Table 5. Results of the grid independent test.

S. no.	Number of the elements	Nusselt number	Percentage variation of Nusselt Number (Nu)
1	4.375×10^5	100.34	-
2	6.25×10^5	98.53	1.81
3	1.75×10^6	97.92	0.62
4	2.51×10^6	97.13	0.81

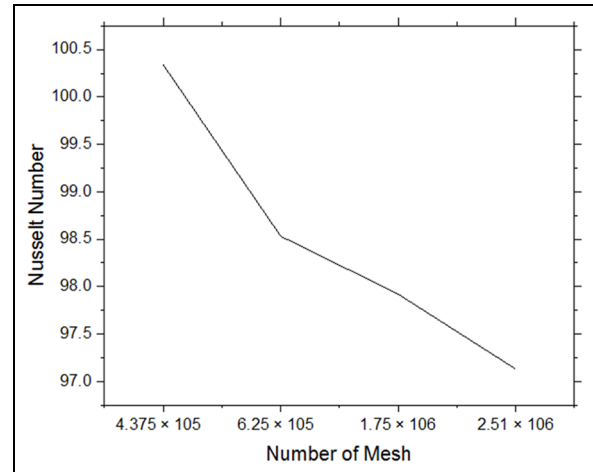
**Figure 6.** Grid independence test.

Table 5 shows that at number of the element 4.375×10^5 , 6.25×10^5 , 1.75×10^6 , and 2.51×10^6 the percentage variation in Nusselt Number is 1.81%, 0.62% and 0.81% which shows the minimum variation occur at the number of the element of 1.75×10^6 . So for further simulation selected the number of the element is 1.75×10^6 . The graphical representation of the grid independence test is give in Figure 6.

The solid and the fluid domain are the two zones that have been analyzed in the CFD simulation. The absorber plate represents the solid zone made of copper material with a plate thickness of 1 mm. The length and the width of the absorber plate are 180×92 cm. the triangular fins are fixed on the absorber plate with a base of 5 cm and a height of 2.54 cm. The pitch of the triangular fins is 9 cm.

Experimental set up

Figure 7 shows the simple solar air heater with triangular fins (SSAHF). The triangular fins are used for increasing the HT between the AP and air. A total of 94 triangular fins of height 2.54 cm and a base width of 5 cm were used on the absorber plate in a staggered pattern. The one fin base center to the other fin base center distance was maintained to be 9 cm (pitch). Figure 8 shows the schematic representation of the

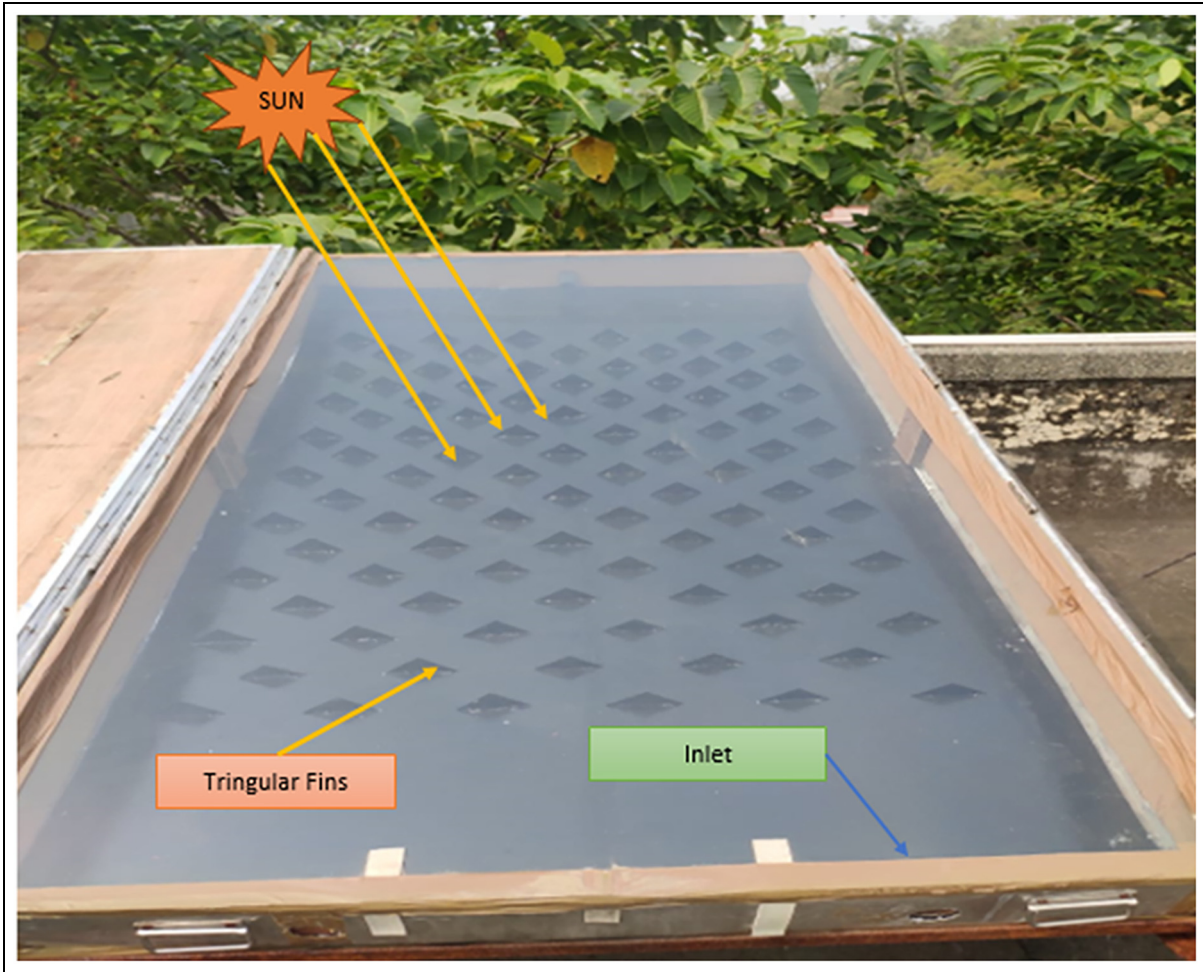


Figure 7. Triangular type finned SAH.

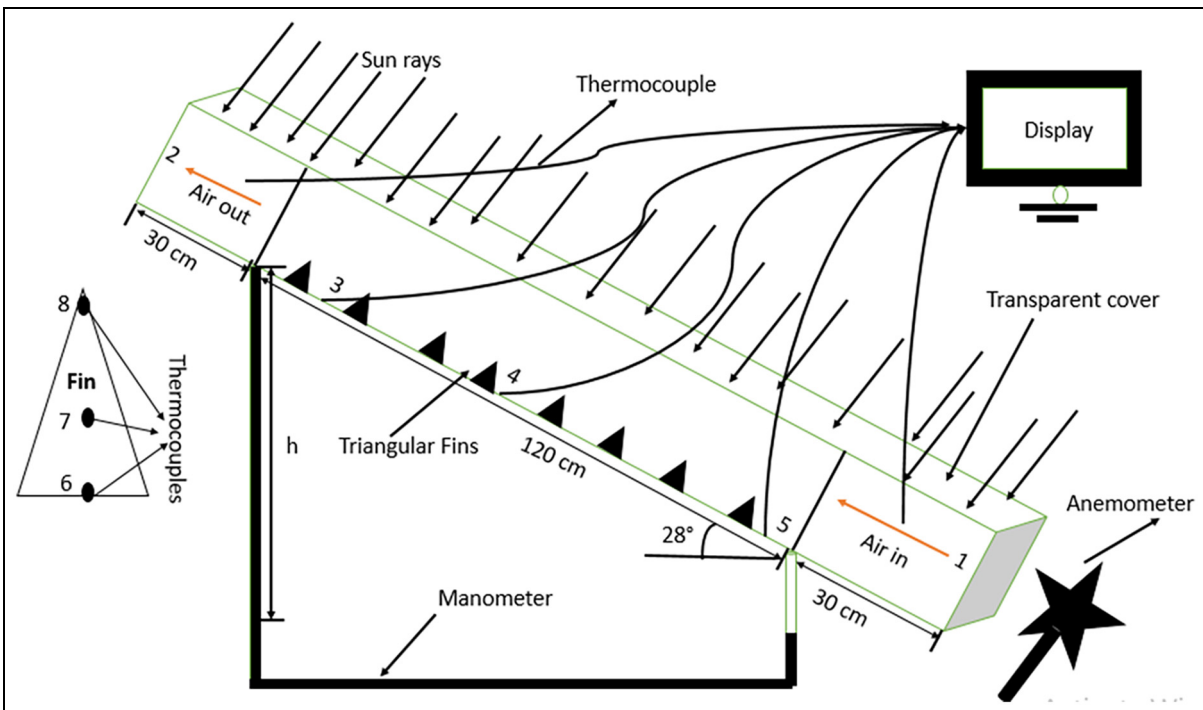


Figure 8. Schematic representation of experimental set up.

experimental setup of SSAHF. The tampered glass temperature has been measured by the non contact temperature measuring device, the inlet and outlet air temperature have been measured by the fixing the thermocouple at inlet and outlet flow section of the SAH (1, 2). The absorber plate temperature is measured by fixing the three thermocouple one at the top, second at the mid and third at the bottom of the absorber plate (3,4,5). The temperature in the direction of the height of the fin is measured by fixing the thermocouple at the base, mid and top of the fin (6,7,8). The anemometer is used for measuring the inlet air velocity. Which is further used for measuring the MFR of air. The U-tube mercury-filled glass tube is used for measuring the pressure drop along the length of SAH. The instruments used in the experimental work is represented in Figure 9. The Figure 9(a)–(d) represents the Anemometer, 8 channel thermocouple connector, pyranometer (solar Flux measurement) and non-contact temperature measuring device.

The SAH has been inclined at 28° from horizontal (Latitude of Bareilly, Uttar Pradesh, India). It is already assumed that the temperature in the direction of the width of AP remains constant. So average temperature (T_p) of AP has been determined by the average temperature of the thermocouple placed at the top, bottom, and middle part of SAH. The average

temperature of the AP helps to determine the heat transfer coefficient and total heat transfer by the SAH. The further efficiency of SAH has been determined by the (32). The exergetic efficiency of SAH has been determined by equation in Figure 13 after measuring the outlet and inlet air temperature.

Uncertainty analysis

The numerical results of SAH has been validated with experimental results after collecting the experimental data and performance parameters. The inlet air velocity has been determined by the anemometer as shown in Figure 7(a) and the inlet air velocity is used to calculate, the mass flow rate of the air. The inlet and outlet temperatures of air is measured by the thermocouples located at inlet and outlet section of SAH which are further used for determining the useful heat gain by the air. The absorber plate average temperature is used for determining, the heat loss and loss in exergy from the SAH. These input variables data has been measured by the instruments which always have some uncertainty that will further increases the inaccuracy of the response parameters. The inaccuracy of the responses depend on the model equations.⁴¹ So following are the model equations used for determining the accuracy of the output parameters.

The efficiency of SAH is the function of $\eta_I = f(S, T_{out}, T_{in}, m)$, so the uncertainty equation of solar air heater efficiency.

$$y_{\eta_I} = \sqrt{\left(\frac{\partial \eta_I}{\partial m}\right)^2 y_m^2 + \left(\frac{\partial \eta_I}{\partial T_{out}}\right)^2 y_{T_{out}}^2 + \left(\frac{\partial \eta_I}{\partial T_{in}}\right)^2 y_{T_{in}}^2 + \left(\frac{\partial \eta_I}{\partial S}\right)^2 y_S^2} \quad (15)$$

The solar air heater's exergy efficiency $\eta_{II} = f(S, m, T_{out}, T_{in}, P_{out}, P_{in})$, So uncertainty in exergy efficiency is represented by the following equation. So uncertainty in the exergy efficiency is

$$y_{\eta_{II}} = \sqrt{\left(\frac{\partial \eta_{II}}{\partial m}\right)^2 y_m^2 + \left(\frac{\partial \eta_{II}}{\partial T_{out}}\right)^2 y_{T_{out}}^2 + \left(\frac{\partial \eta_{II}}{\partial T_{in}}\right)^2 y_{T_{in}}^2 + \left(\frac{\partial \eta_{II}}{\partial P_{in}}\right)^2 y_{P_{in}}^2 + \left(\frac{\partial \eta_{II}}{\partial P_{out}}\right)^2 y_{P_{out}}^2 + \left(\frac{\partial \eta_{II}}{\partial S}\right)^2 y_S^2} \quad (16)$$

The exergy destruction is also the function of the MFR, solar intensity, an inlet temperature of atmospheric air, the outlet temperature of atmospheric air, inlet air pressure, and outlet air pressure. So uncertainty equation in the exergy destruction is represented by the following equation.

$$y_{E_d} = \sqrt{\left(\frac{\partial E_d}{\partial m}\right)^2 y_m^2 + \left(\frac{\partial E_d}{\partial T_{out}}\right)^2 y_{T_{out}}^2 + \left(\frac{\partial E_d}{\partial T_{in}}\right)^2 y_{T_{in}}^2 + \left(\frac{\partial E_d}{\partial P_{in}}\right)^2 y_{P_{in}}^2 + \left(\frac{\partial E_d}{\partial P_{out}}\right)^2 y_{P_{out}}^2 + \left(\frac{\partial E_d}{\partial S}\right)^2 y_S^2} \quad (17)$$



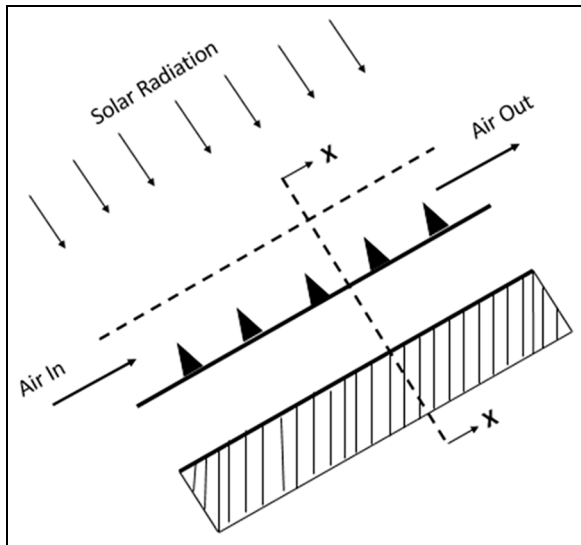
Figure 9. Instruments used in experimental work: (a) anemometer, (b) 8 channel thermocouple connector, (c) pyranometer, and (d) multi thermometer.

The inlet and outlet air temperature have been measured by the thermocouple with $\pm 4.25\%$ accuracy, the inlet velocity of air has been measured with the

help of an anemometer with an accuracy of $\pm 4\%$, and the MFR is calculated by the air entering velocity. The PD has been calculated by U tube inclined

Table 6. Uncertainty in input parameters.

S. no.	Parameter	Instruments	Uncertainty(%)
1	Temperature measurement	Thermocouples	4.25
2	Pressure measurement	Manometer	4.10
3	Velocity measurement	Anemometer	4
4	Solar Intensity	Pyranometer	4.89
5	Mass Flow Rate	-	4.24
6	Solar air heater efficiency	-	3.56
7	Exergy efficiency	-	4.10
8	Exergy destruction	-	4.89

**Figure 10.** Schematic representation of finned SAH.

manometer of accuracy $\pm 4.10\%$, and the solar intensity is measured by the pyranometer with an accuracy of 4.89% . So the total uncertainty of input and output parameters is given in Table 6.

Modell equation for energy and exergy analysis of SAH

The model equations are used for determining the thermal, thermal hydraulic performance and exergy analysis of the SAH. The thermal analysis is used for determining the efficiency and various heat interaction with SAH. The thermal hydraulic performance analysis is used for determining the pressure drop, friction factor and blower power. The exergy analysis represents the real performance analysis.

Figure 10 represents the schematic representation of the finned SAH. In this SAH, the air is flowing over the black painted absorber plate, above of the absorber plate transparent cover is provided. Figure 11 represents the block diagram of the solar flux intensity calculation and thermal performance analysis of the SAH. Figure 11 clearly shows that the solar

flux radiation at particular place depends on the day of the year, latitude, surface azimuth angle and the hour angle.

Figure 12 represents the thermal network circuit diagram for determining the heat loss from the absorber plate in the atmosphere. In this analysis it is assumed that the heat transfer through sides and bottom of SAH is neglected.

It can be clearly seen from Figure 12 is that heat flow from the absorber plate to the cover plate and further transfer to the atmosphere by convection and radiation. The total heat transfer from the absorber plate to the atmosphere is determined by following relation.

$$Q_{Losses} = \frac{T_p - T_{atm}}{R_{eq}} \quad (18)$$

The T_p and T_{atm} represents the absorber plate and atmospheric temperature. The R_{eq} represents the equivalent resistance in the thermal circuit analysis. Further the R_{eq} calculated by following equation.

$$R_{eq} = R_{eq1} + R_{eq2} \quad (19)$$

$$R_{eq} = \frac{R_1 R_2}{R_1 + R_2} + \frac{R_3 R_4}{R_3 + R_4} \quad (20)$$

The R_1 and R_2 represents the convection and radiation resistance between the absorber plate and the cover plate. The R_3 and R_4 are the thermal resistance of convection and radiation between the transparent cover and the atmospheric.

The convection resistance absorber plate and tempered glass has been given by following equation

$$R_1 = \frac{1}{hcA_p} \quad (21)$$

The radiation resistance between the absorber plate and the tempered glass is represented by following equation represented in Ref.⁴²

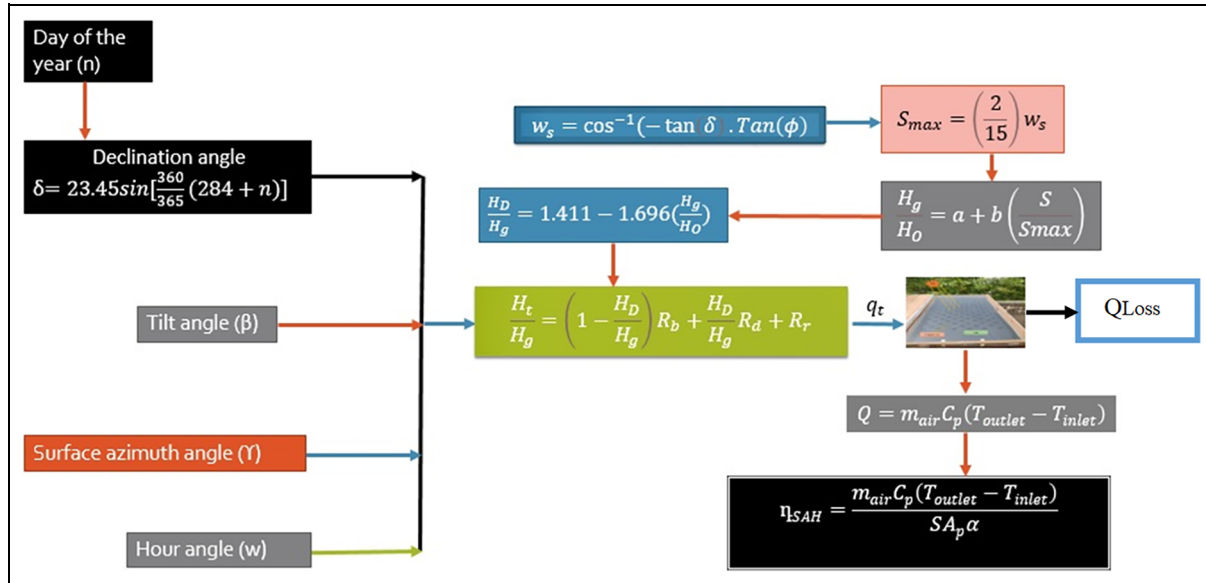


Figure 11. Solar air heater solar flux and thermal efficiency calculation block diagram.

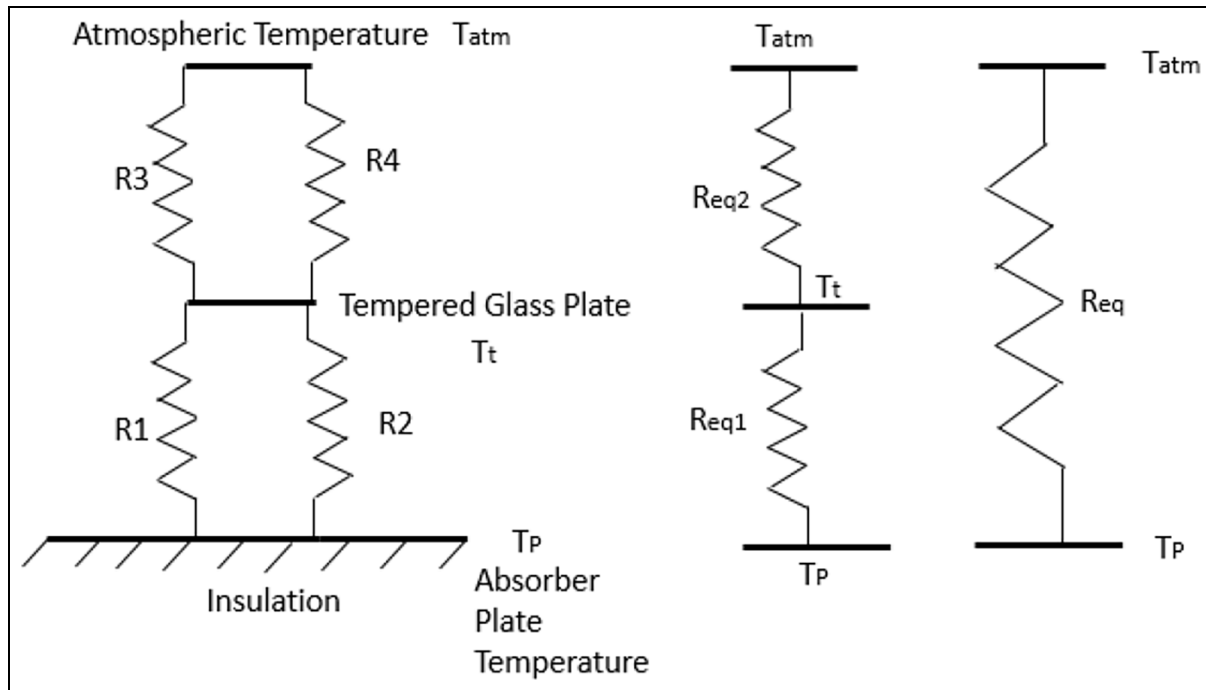


Figure 12. Thermal network of the heat transfer through SAH.

$$R_2 = \frac{\frac{1}{\epsilon_p} + \frac{1}{\epsilon_{tg}} - 1}{\sigma A_p (T_p + T_{tg}) (T_p^2 + T_{tg}^2)} \quad (22)$$

$$R_3 = \frac{1}{h_{tc} A_{tg}} \quad (23)$$

$$R_4 = \frac{\frac{1}{\epsilon_{tg}}}{\sigma A_{tg} (T_{atm} + T_{tg}) (T_{atm}^2 + T_{tg}^2)} \quad (24)$$

Where h_c represents the convection heat transfer coefficient air on absorber plate and the ϵ_p and ϵ_{tg} represents the emissivity of the absorber plate and the tempered glass. The T_p and T_{tg} are the absorber plate and the tempered glass cover temperature. The same way R_3 and R_4 represented by the following equations.

The h_{tc} and A_{tg} represents the convection heat transfer coefficient between the tempered glass and the air and tempered glass surface area. The T_{atm} and T_{tg}

represents the atmospheric temperature and the tempered glass temperature.

In above equations the heat transfer coefficient of air with absorber plate and the air with tempered glass are different but for calculation purpose it is assumed to be equal.

$$h_c = h_{Tgc} \quad (25)$$

These are calculated by the following Nusselt Number correlation.

$$Nu = 0.35 \left(\frac{F_T}{F_L} \right)^{0.2} Re^{0.6} Pr \left(\frac{P_r}{P_{rs}} \right)^{0.25} \quad 1000 < Re < 2 \times 10^5 \quad (26)$$

$$Nu = 0.035 \left(\frac{F_T}{F_L} \right)^{0.2} Re^{0.8} Pr \left(\frac{P_r}{P_{rs}} \right)^{0.25} \quad 2 \times 10^5 < Re < 2 \times 10^6 \quad (27)$$

Where F_L , F_T , and F_D are the longitudinal, transverse, and diagonal pitch of the fin arrangements. In equations (26) and (27) Re and Pr represent the non-dimensional Reynolds Number and Prandtl number respectively. The Re and Pr values have been calculated on the arithmetic temperature of the air but Pr_s is the Prandtl number calculated at the surface temperature of the fins.

The air properties have been selected to be the average temperature of the air as presented in Ref.⁴³

$$T_{average} = \frac{T_{inlet} + T_{outlet}}{2} \quad (28)$$

T_{inlet} and T_{outlet} are the inlet and outlet temperatures of the air in the SAH.

Due to fixing of the triangular fins on the absorber plate significant improvement of the heat transfer and pressure drop occur. So actual enhancement in heat transfer due to roughness has been calculated by the Thermal Performance Factor (TPF). The TPF is the ratio of the enhancement of Nusselt Number due to finned surface to the enhancement of the friction factor as compared to smooth surface. The following equation has been used for the calculation of the TPF on the finned surface.

$$TPF = \frac{\frac{Nu_{finned}}{Nu_{smooth}}}{\frac{f_{finned}}{f_{smooth}}} \quad (29)$$

The Nusselt Number on the smooth surface is calculated by the Dittus-Boelter equation.⁴⁴

$$Nu_{Smooth} = 0.023 Re^{0.8} Pr^{0.4} \quad (30)$$

The friction factor is calculated by modified Blasius equation.⁴⁴

$$f_{smooth} = 0.085 Re^{-0.25} \quad (31)$$

The efficiency of the SAH represented by following equation.

$$\eta_{SAH} = \frac{m_{air} C_p (T_{outlet} - T_{inlet})}{q_t A_p \alpha} \quad (32)$$

Where m_{air} is the mass flow rate of air, C_p is the constant pressure specific heat of air, T_{outlet} is the outlet temperature of air, and T_{inlet} is the inlet temperature of air. S is the solar flux and α is the absorptivity of the absorber plate.

Exergy analysis of the solar air heater

Exergy analysis in a thermal system represents the real analysis, it counted the effect of the electric power consumed by the blower. Figure 13 represents the exergy flow block diagram in which the total exergy supplied is the sum of exergy supplied by the Sun and the electric power consumed by the blower. The loss in exergy takes place due to irreversibility present inside the SAH and exergy losses in the atmosphere due to temperature difference between system and surrounding. The total exergy recovered is the gain in the exergy of the air due to increase in air temperature. Now finally, exergy efficiency is the ratio of the exergy recovered to the exergy supplied.

Optimization technique

Response Surface Methodology (RSM) is the optimization technique that has been used for optimizing the experimental setup. It was first time used by K. B. Wilson and George E. P. Box.⁴⁵ It defined the relation among the response variables and input variables. It reduced the experimental time by maintaining the proper sequencing of experimental sets to obtain the optimal solution. The Box and Wilson used the second order polynomial since it saves the time and the easy to follow the process even little knowledge of the path.⁴⁶ RSM is very useful tool of the optimization as compared to other optimization techniques since it consume less time, it easily convert the experimental data of the input and responses in terms of the second order polynomial. The beauty of the second order polynomial is that it can easy to apply, even little knowledge of the process. The steps of RSM represented in Figure 14.

In this research article Central Composite Design (CCD) technique has been used for the Design of Experiment (DoE). In this method, minimum and maximum value of input variables have been provided and which affects the total number of runs given in Table 1.

The friction factor, Nusselt Number and TPF is an important parameter for determining the pressure

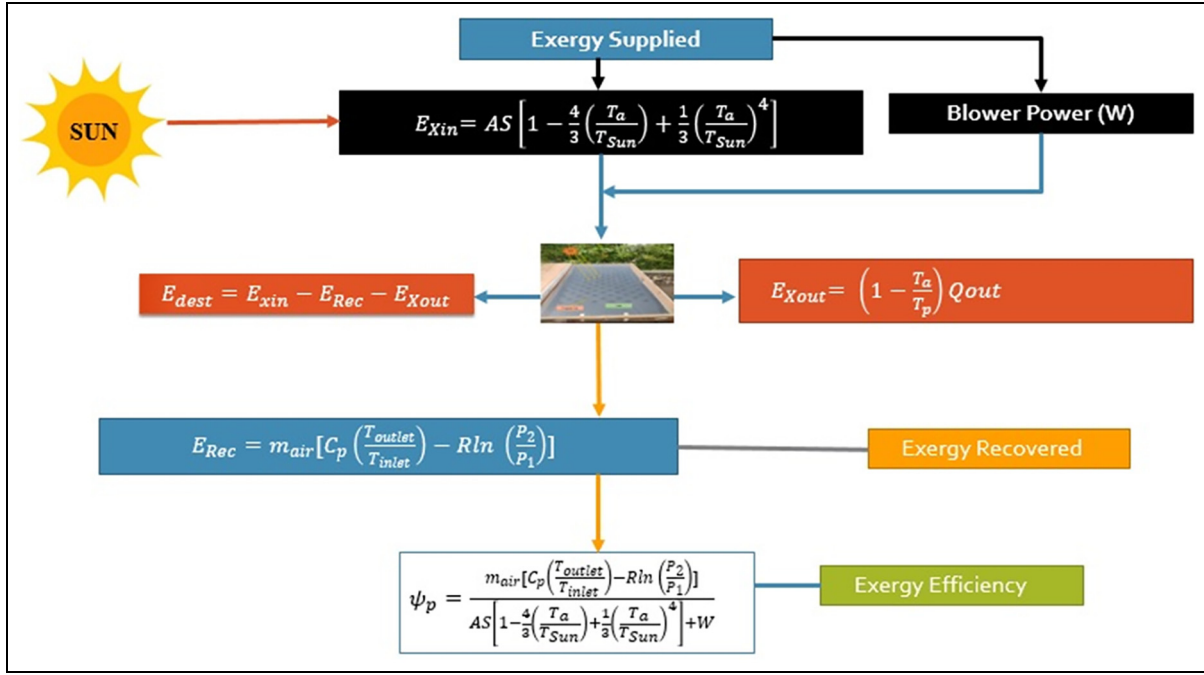


Figure 13. Block diagram of exergy analysis of the SAH.

drop, heat transfer, and enhancement of heat transfer with respect to pressure drop on the surface of SAH. These parameters depends on the Reynolds number and the geometry of the fins. The following regression equations have been generated in the two-degree polynomial of the responses.

$$f = 0.053042 - 0.00000290345Re - 0.00189 \left(\frac{P}{L} \right) + 0.000000000830435(Re)^2 + 0.000098 \left(\frac{P}{L} \right)^2 + 0.000000277829(Re) \left(\frac{P}{L} \right) \quad (33)$$

$$Nu = 16.05279 - 0.011312Re - 5.60573 \left(\frac{P}{L} \right) - 0.000000608850(Re)^2 + 0.617768 \left(\frac{P}{L} \right)^2 - 0.000315(Re) \left(\frac{P}{L} \right) \quad (34)$$

$$TPF = 1.69854 + 0.000032Re - 0.019982 \left(\frac{P}{L} \right) - 0.0000000105(Re)^2 + 0.000313 \left(\frac{P}{L} \right)^2 - 0.00000075(Re) \left(\frac{P}{L} \right) \quad (35)$$

The regression analysis have been formed by Analysis of Variance (ANOVA) in MINITAB-17 software.

Table 7 represents the total number of experimental runs and corresponding values of the responses. The input variables selected for analysis are Reynolds Number and Pitch to height ratio. The selected responses are Nusselt Number, friction factor and TPF. The Table 8 represents the Analysis of Variance (ANOVA) table of Nusselt Number which shows the values of p and F parameters. The p and F values decided the effectiveness of ANOVA analysis. Table 8 clearly shows that the p values are less than 0.0001 which shows the Model for Nusselt Number is significant. Similar manner Tables 9 and 10 shows that model are significant since values of p is less than 0.0001. The F values in Tables 8 to 10 is large which also shows model is validated with good effectiveness.

Tables 11 to 13 shows the error analysis of the Nusselt Number, friction factor and the TPF. The Tables 11 to 13 shows the adjusted and Predicted R^2 values for Nusselt Number, Friction factor and TPF are namely 0.9995 and 0.9981, 0.9846 and 0.9363, and 0.9533 and 0.8243 respectively. The adjusted and predicted R^2 values are very close to one. So, it can concluded that the correlation represented by the equations (33)–(35) have been accurated and acceptable within the range of input variables.

Result and discussion

Velocity contour

Figure 15 represents the velocity contour at an air inlet velocity of 0.5 m/s but the maximum velocity in between the gap of fins is 0.587 m/s. The maximum velocity over the solar air heater is higher than the inlet

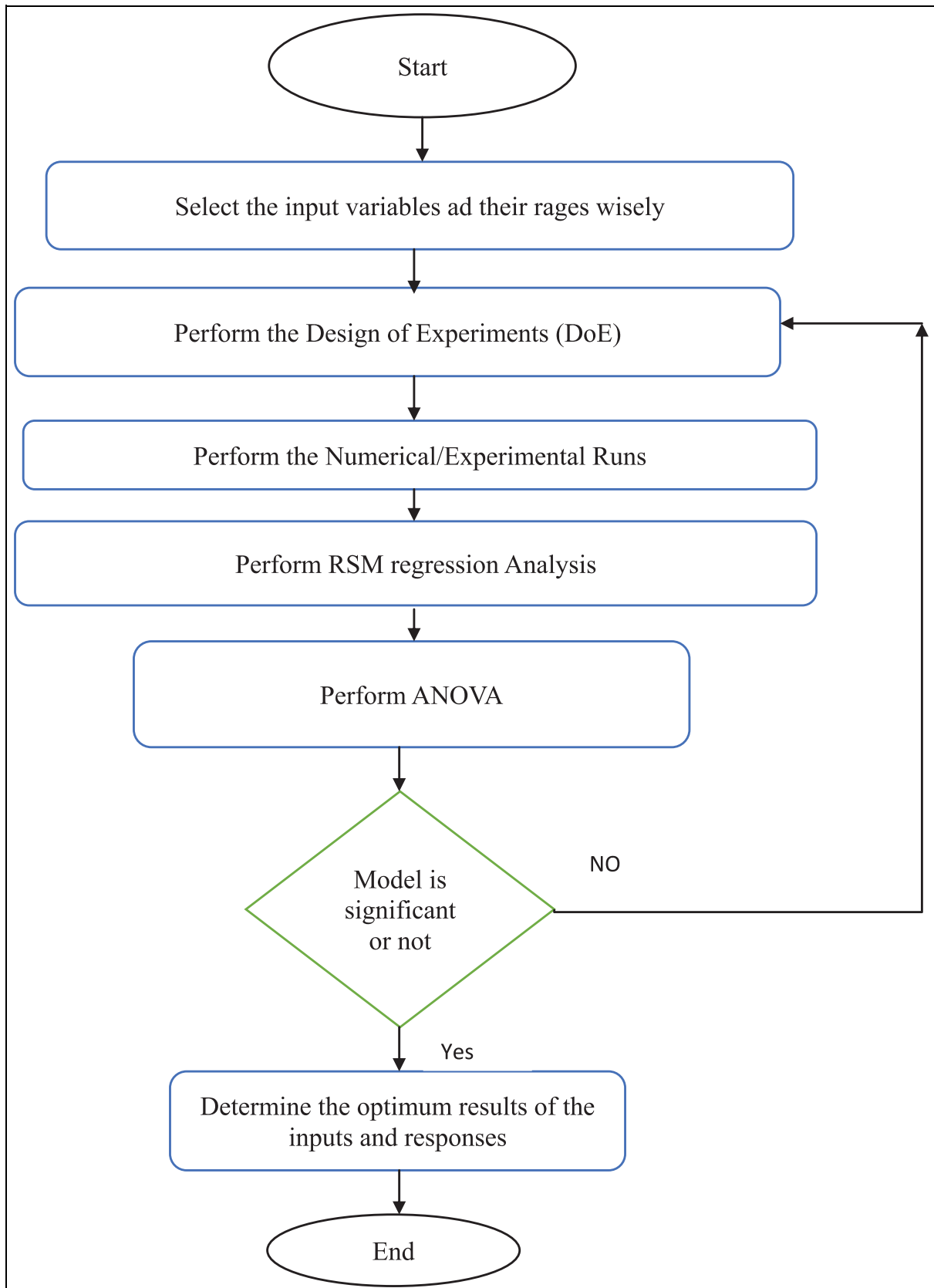


Figure 14. Steps followed in RSM analysis.

Table 7. Total number of experimental runs and corresponding responses.

S. no.	Re	P/L	Nu	f	TPF
1	5000	6	50.35	0.032857685	1.7
2	5000	2	58.039	0.036612839	1.8
3	10,000	6.82	91.38	0.025998919	1.74
4	10,000	4	97.92	0.0274052	1.81
5	10,000	4	97.92	0.0274052	1.801
6	10,000	4	97.92	0.0274052	1.812
7	2928.93	4	33.073	0.040566358	1.69
8	10,000	4	97.92	0.0274052	1.801
9	17,071.06	4	157.11	0.023101964	1.8
10	10,000	4	97.92	0.0274052	1.801
11	15,000	2	153.28	0.025777505	1.89
12	10,000	1.17	114.77	0.030928731	1.86
13	15,000	6	132.98	0.023133665	1.76

Table 8. ANOVA tables of the Nusselt Number.

Source	Sum of square	df	Mean square	F-Value	p-Value	
Model	16175.30	5	3235.06	5193.29	< 0.0001	Significant
A-Reynolds Number (Re)	15602.82	1	15602.82	25047.43	< 0.0001	
B-P/L	466.16	1	466.16	748.33	< 0.0001	
AB	39.77	1	39.77	63.84	< 0.0001	
A ²	16.12	1	16.12	25.87	0.0014	
B ²	42.48	1	42.48	68.19	< 0.0001	
Residual	4.36	7	0.6229			
Lack of fit	4.36	3	1.45			
Pure error	0.0000	4	0.0000			
Cor total	16,179.66	12				

Table 9. ANOVA table of the friction factor.

Source	Sum of square	df	Mean square	F- value	p-Value	
Model	0.0003	5	0.0001	154.64	< 0.0001	Significant
A-Reynolds Number (Re)	0.0003	1	0.0003	641.15	< 0.0001	
B-P/L	0.0000	1	0.0000	55.96	0.0001	
AB	3.088E-07	1	3.088E-07	0.7732	0.4084	
A ²	0.0000	1	0.0000	75.08	< 0.0001	
B ²	1.063E-06	1	1.063E-06	2.66	0.1468	
Residual	2.795E-06	7	3.993E-07			
Lack of Fit	2.795E-06	3	9.318E-07			
Pure Error	0.0000	4	0.0000			
Cor total	0.0003	12				

Table 10. ANOVA table of TPF.

Source	Sum of square	df	Mean square	F- value	p-Value	
Model	0.0368	5	0.0074	50.03	< 0.0001	Significant
A-Reynolds Number (Re)	0.0117	1	0.0117	79.30	< 0.0001	
B-P/L	0.0200	1	0.0200	135.68	< 0.0001	
AB	0.0002	1	0.0002	1.53	0.2562	
A ²	0.0048	1	0.0048	32.57	0.0007	
B ²	0.0000	1	0.0000	0.0738	0.7937	
Residual	0.0010	7	0.0001			
Lack of Fit	0.0009	3	0.0003	9.93	0.0252	
Pure Error	0.0001	4	0.0000			
Cor total	0.0378	12				

Table 11. ANOVA error analysis for Nusselt number.

S. no	Source	Sequential p -values	Adjusted R^2	Predicted R^2
1	Linear	< 0.0001	0.9918	0.9850
2	2FI	0.0513	0.9942	0.9900
3	Quadratic	< 0.0001	0.9995	0.9981
4	Cubic	0.0019	0.9999	0.9986

Table 12. ANOVA error analysis for friction factor.

S. no	Source	Sequential p -values	Adjusted R^2	Predicted R^2
1	Linear	< 0.0001	0.8722	0.8031
2	2FI	0.7779	0.8593	0.7739
3	Quadratic	0.0002	0.9846	0.9362
4	Cubic	0.0225	0.9953	0.8741

Table 13. ANOVA error analysis for TPF.

S. no	Source	Sequential p -values	Adjusted R^2	Predicted R^2
1	Linear	0.0001	0.8033	0.6738
2	2FI	0.5749	0.7894	0.6649
3	Quadratic	0.0021	0.9533	0.8243
4	Cubic	0.2297	0.9637	0.2340

air velocity due to a reduction in the area of the flow between the fins as per the equation (20). The maximum air velocity is 1.17 m/s when inlet air velocity is 1 m/s and when air inlet velocity is increased to 1.5 m/s the maximum air velocity reached 1.754 m/s.^{22,23}

Pressure contour

The pressure drop is represented by momentum equations (2)–(4) as the total pressure drop is contributed by the form drag coefficient and the skin friction coefficient. The form drag coefficient is assumed to be constant at 1.2⁴⁷ and the skin friction coefficient is determined by calculating the pressure drop.

Figure 16(a)–(c) represents the pressure drop at varying inlet air velocity. The air inlet velocity changes from 0.5, 1, and 1.5 m/s then pressure drop increase from the 0.15, 0.536, and 1.16 Pa. Most of the pressure drops occur by the direct impact of the air on the triangular surfaces.⁴⁸

Temperature contour

Figure 17(a)–(c) represents the temperature distribution on the surface of SAH. The temperature distribution is based on the Roserland radiation model. So with the help of this model, the temperature field is easily determined during the months of the summer season at 10 AM, 11 AM, and 12 PM. In Figure 17(a)–(c) the maximum temperature of the copper

plate is 335 K, 379 K, and 382.5 K. The air outlet temperature reached to be 313 K, 351 K, and 357 K with respect to the air inlet temperature of 300 K.^{48,49}

3D streamlines in the solar air heater

Figure 18 shows the 3D streamlines flow in SAH. The streamlines are very important for representing the flow in the form of flow lines. The bottom part of SAH have high turbulence due to obstruction produced by the triangular fins. The turbulence in the SAH improves the heat transfer to the air by the AP.⁴⁹

Turbulence kinetic energy and turbulence eddy dissipation

The k- ϵ model represents the turbulence kinetic energy presented by the model equations (9) and (10). Figure 19(a) represents the turbulence kinetic energy of the air in between the fin's surface, the maximum turbulence obtained is 0.030 m²/s² in the gap between the absorber plate and the glass cover. The turbulence is very much required for promoting the heat transfer between the AP and air.⁵⁰ The high turbulence is created due to obstruction presented by the triangular fins. The flowing air suddenly stopped due to obstruction produced by the triangular fins and create turbulence near the fin's surface. So, turbulence increase the heat transfer in the air.

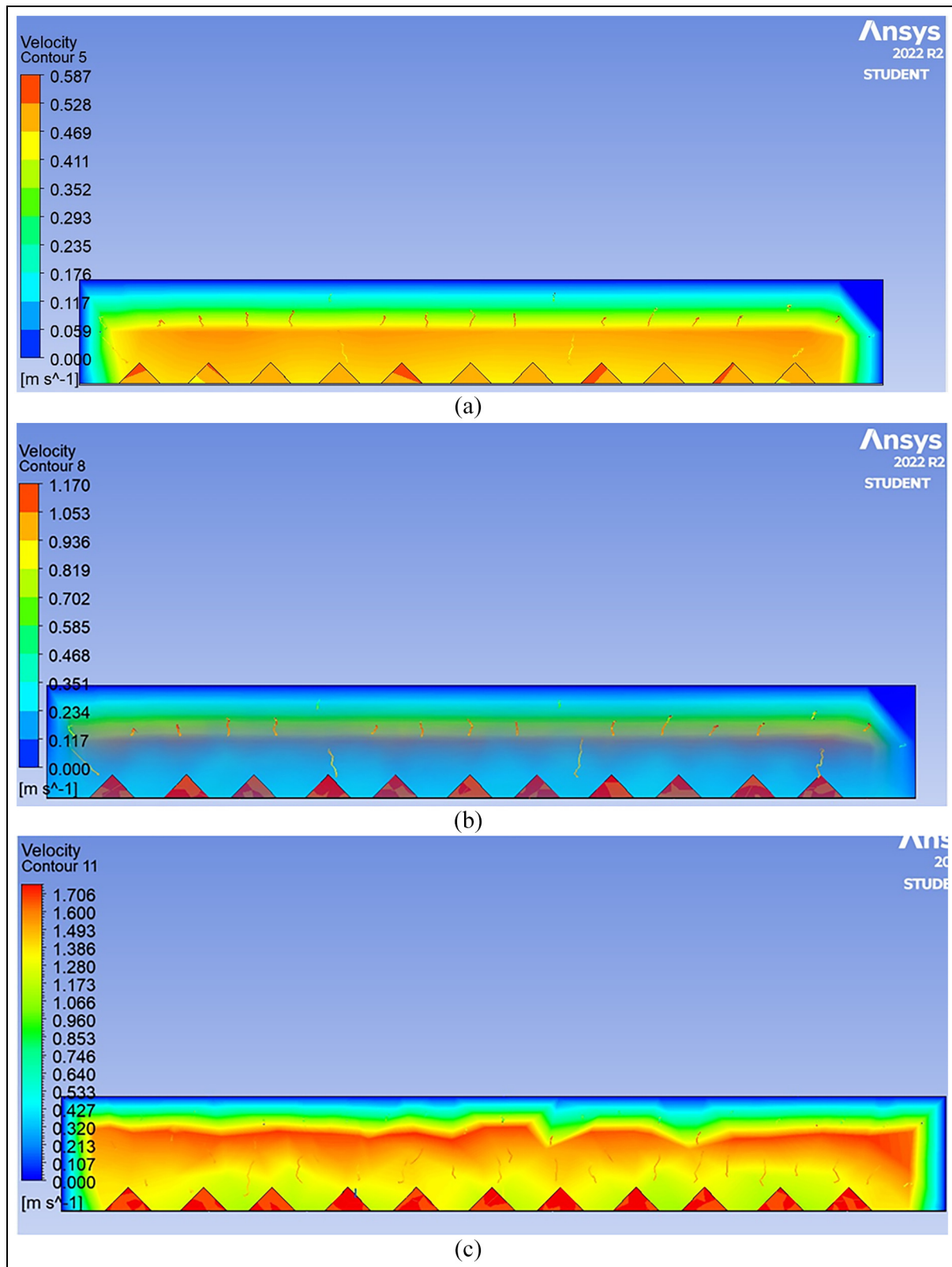


Figure 15. Velocity distribution in SAH: (a) velocity contour at inlet air velocity at 0.5 m/s at 10 AM in summer season, (b) velocity contour at inlet air velocity 1 m/s 11 AM in summer season, and (c) velocity contour at inlet air velocity 1.5 m/s at 12 PM in the summer season.

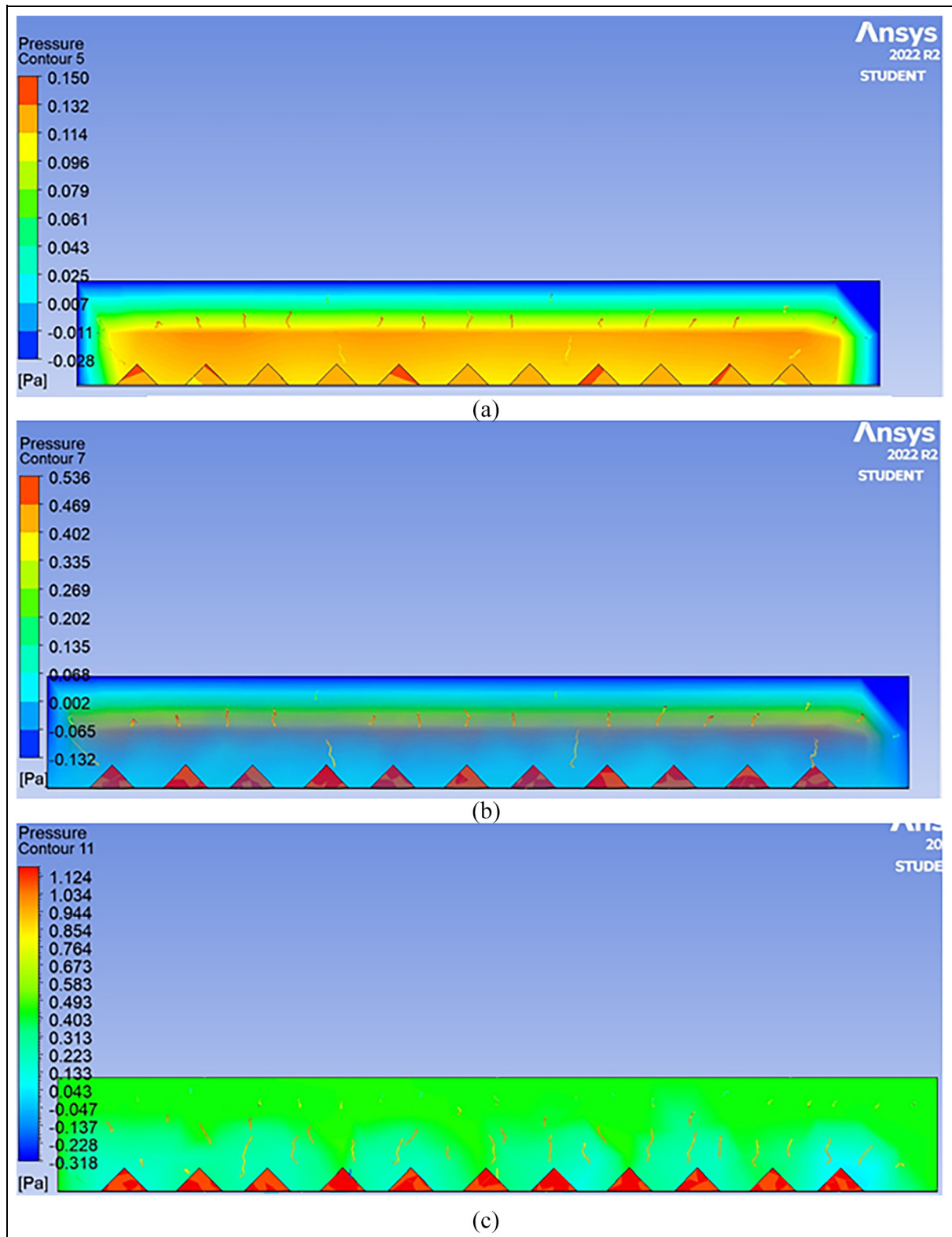


Figure 16. Pressure drop over the surface of the AP: (a) pressure contour at inlet air velocity 0.5 m/s at 10 AM in the summer season, (b) pressure contour at inlet air velocity 1.0 m/s at 11 AM in the summer season, and (c) pressure contour at inlet air velocity 1.5 m/s at 12 PM in the summer season.

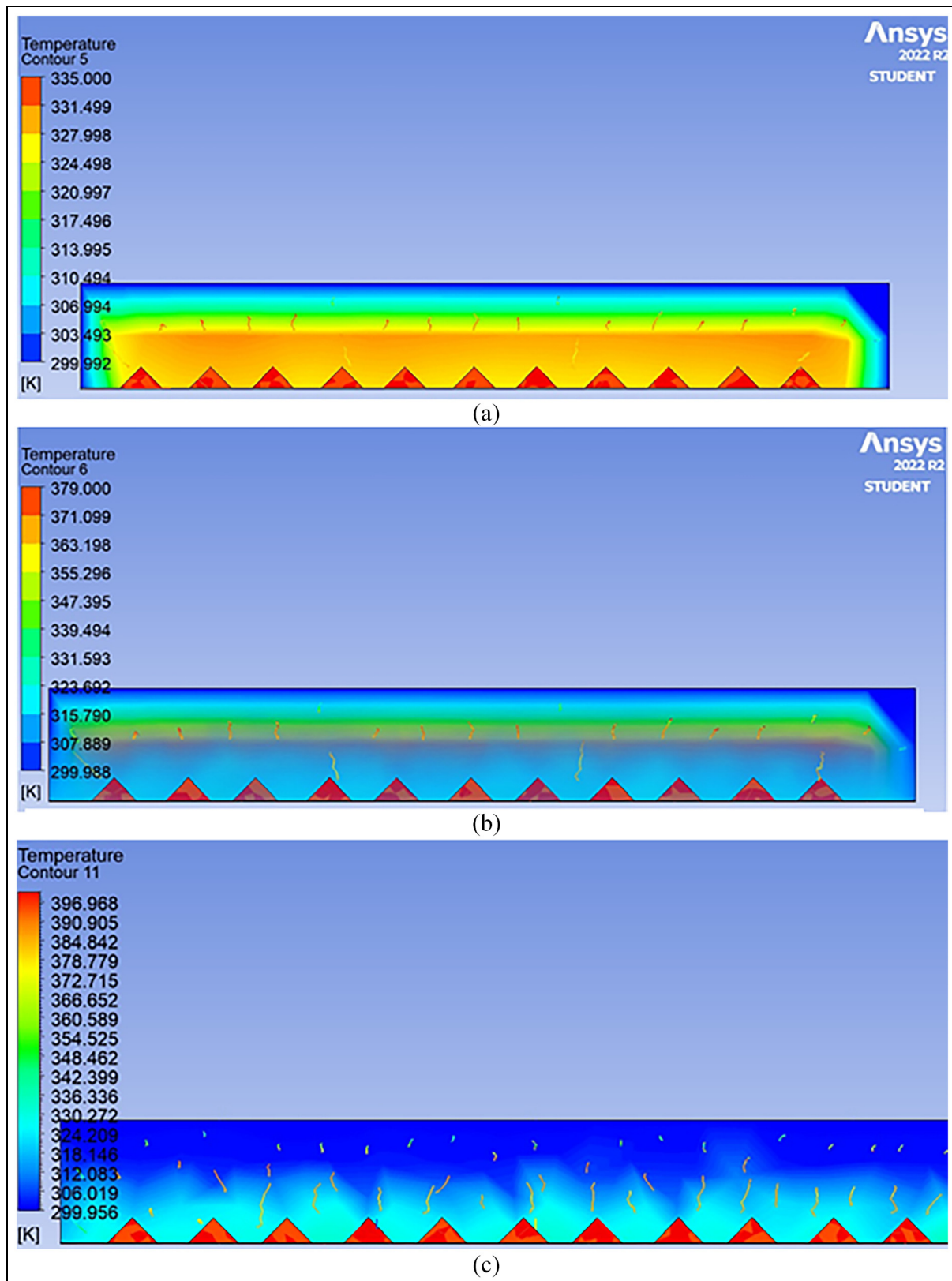


Figure 17. Temperature contour on the SAH AP: (a) temperature contour at inlet air velocity 0.5 m/s at time 10 am in Summer season, (b) temperature contour at inlet air velocity 1 m/s at time 11 AM in Summer season, and (c) temperature contour at inlet air velocity 1.5 m/s at time 12 PM in Summer season.

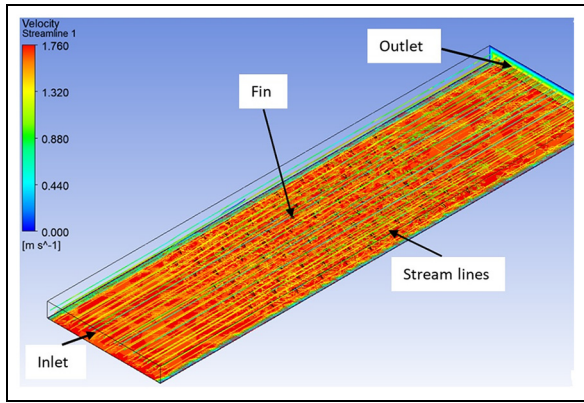


Figure 18. 3D representation of streamlines in SAH.

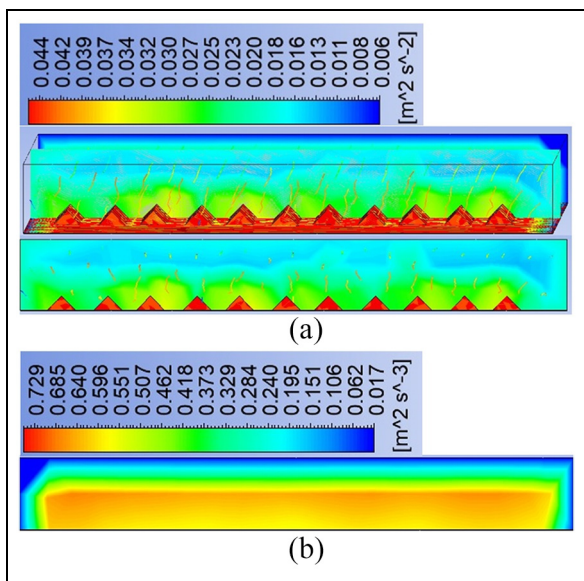


Figure 19. Turbulence kinetic energy and Eddy dissipation: (a) turbulence kinetic energy and (b) Eddy dissipation.

Figure 19(b) shows the eddy dissipation inside the SAH around the triangular fins. The maximum eddy dissipation inside the SAH is $0.729 \text{ m}^2/\text{s}^3$ but very less near to the wall of the SAH namely $0.017 \text{ m}^2/\text{s}^3$.

Temperature variation along the length of the fin

Figure 20 shows the temperature variation along the fin length at a base temperature of 62°C , 106°C , and 109.5°C by soldering the thermocouple at the base to top of the fin at difference of 5 mm. The fin length is 25 mm, so temperature variations show at 0, 5, 10, 15, 20, and 25 mm distance from the base of the fin. Figure 16(a) shows that the when fin base temperature is 62°C then the fin tip temperature is 61.8°C with only a 0.2°C temperature drop between the fin base and tip. In Figure 20(b) the difference between the fin base and tip temperature is 2°C and in Figure 20(c) the temperature difference is 3.5°C . If the fin length increases then the temperature difference between the fin base and the tip is increases but the pressure drop is reduced.

Friction factor, number and TPF variation with input variables

Contour, and surface plot of friction factor. Figure 21(a) shows that if the Reynolds Number increases the friction factor is decreasing since the friction factor is inversely proportional to the Reynolds number as per equation (31). The friction factor is also reduced due to the increase in the P/L ratio since the increase in the Reynolds number and P/L increase the velocity of air which reduces the contact time of air with absorber plate.^{49,51}

Figure 21(b) represents the 2D contour plot of the friction factor with input variables. The blue region in

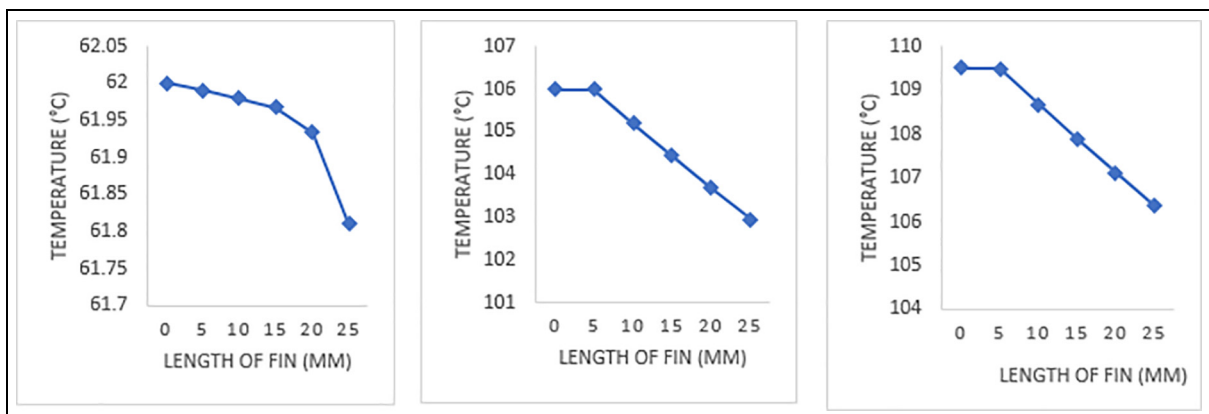


Figure 20. Temperature variation along the length of fins at varying base temperature: (a) temperature variation along the length of the fin at a base temperature of 62°C , (b) temperature variation along the length of the beam at a base temperature of 106°C , and (c) temperature variation along the length of the fin at a base temperature of 109.5°C .

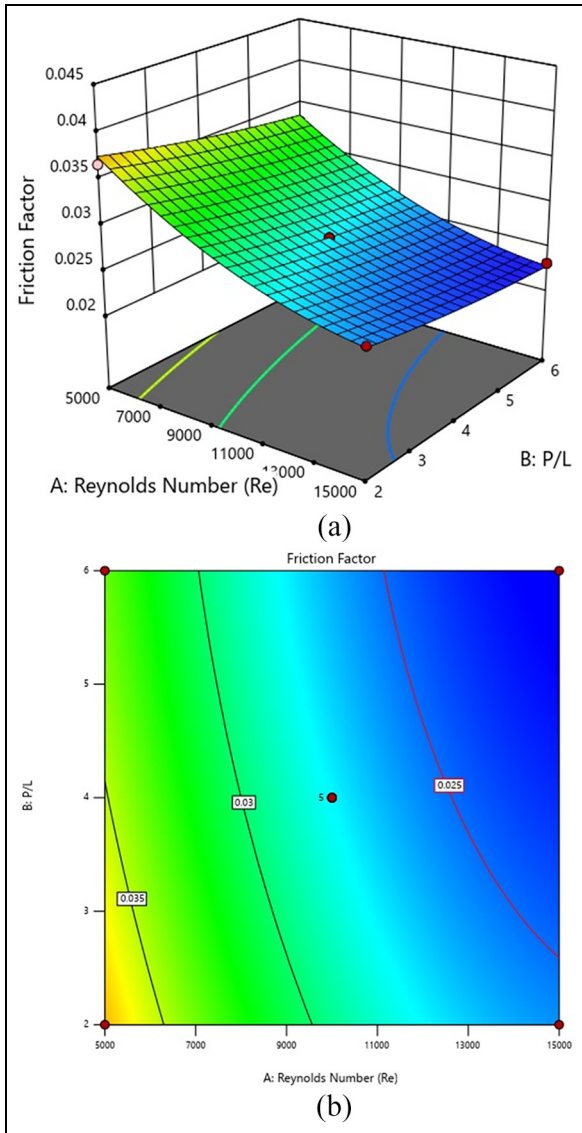


Figure 21. Surface and contour plot of the friction factor with input variables: (a) surface plot of friction factor with input variables and (b) surface plot of friction factor with input variables.

the contour plot represents the lower friction factor, this region is represented by a higher Reynolds number and higher P/L ratio.⁵²

Nusselt number variation with input variables

Nusselt number is the ratio of convective heat transfer within air and the conductive heat transfer between the absorber plate and air at the contact boundary. The ANOVA analysis developed the second order polynomial (34) in terms of the Reynolds number and the P/L ratio.

Figure 22(a) and (b) show the surface and contour plot of the Nusselt number with the input variables. Figure 22(a) shows that if the Reynolds number increase then the Nusselt number increases since

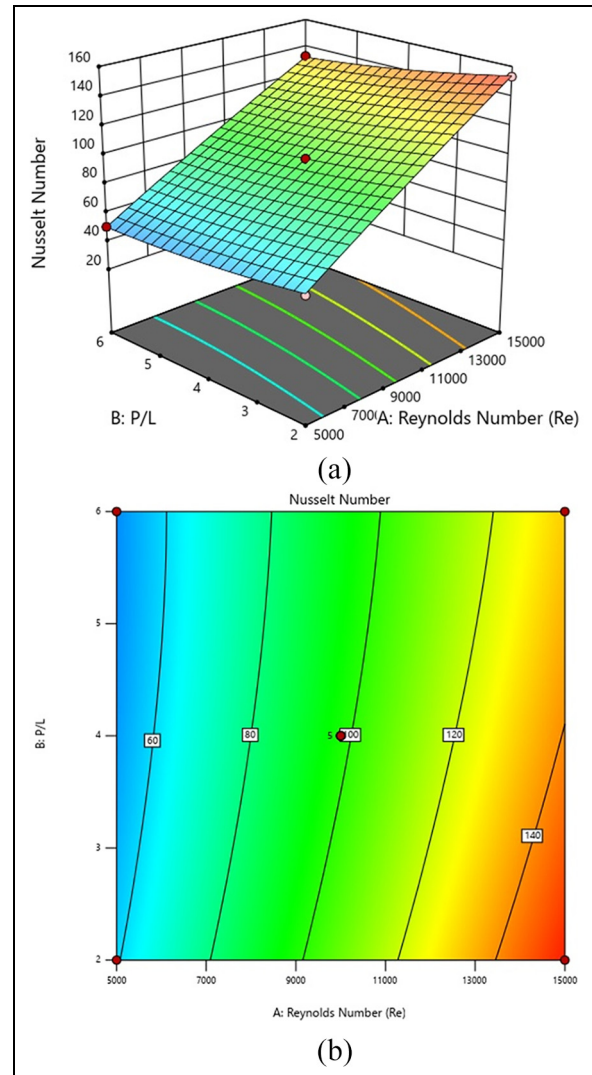


Figure 22. Surface and contour plot of Nusselt Number with input variables: (a) surface plot of Nusselt Number with input variables and (b) contour plot of Nusselt Number with input variables.

enhancement in the Reynolds Number increase the turbulence in the system⁵³ and Figure 22(b) shows that if the P/L ratio increases then Nusselt Number is reduced.

TPF variation with input variables

The TPF values represents the enhancement of heat transfer as compared to pressure drop. Figure 23(a) shows that increase in Reynolds Number increase the TPF values. The enhancement of P/L reduces the TPF values since enhancement in P/L ratio reduces the Nusselt Number. Figure 23(b) shows the contour plot of the TPF with respect the input variables. Figure 23(b) reddish color present the highest values of the TPF, this region represented by the higher Reynolds Number and Lower values of the P/L.

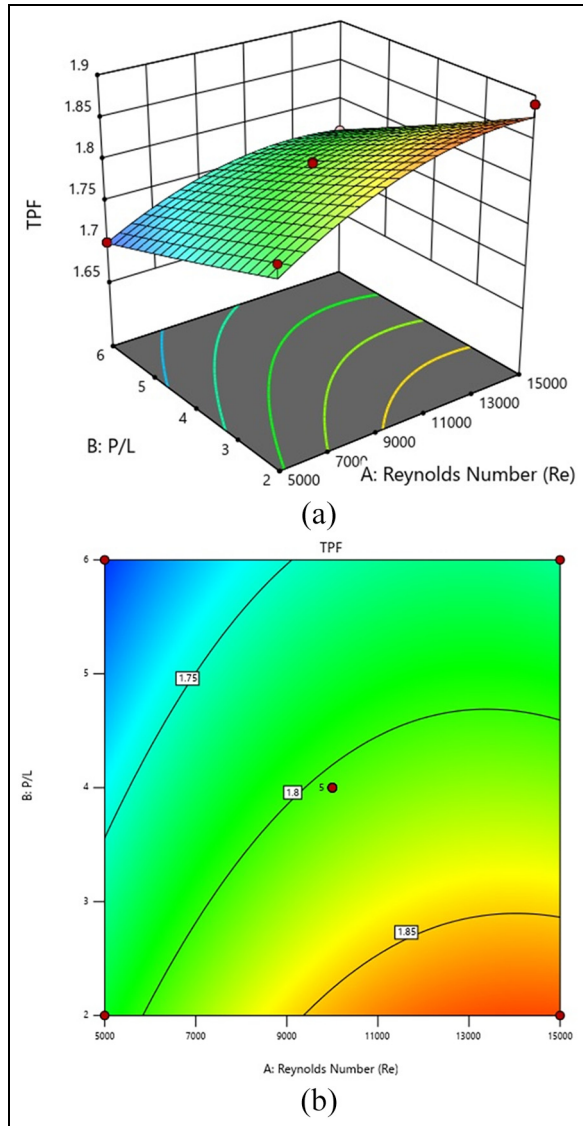


Figure 23. Surface and contour plot of TPF with input variables: (a) surface plot of TPF with input variables and (b) contour plot of TPF with input variables.

Perturbation plot of the response variables with input variables

Figure 24(a)–(c) represents the perturbation plot of responses TPF, friction factor and Nusselt Number with input variables Reynolds Number and P/L ratio. Figure 24(a) shows the perturbation plot of TPF with Reynolds Number and P/L, the slope of the P/L line remain constant but the slope of the Re curve is changes very sharply. The sharp change of the slope shows that the values of Re strongly affects the TPF as compared to p/L ratio. The similar perturbation curve has been seen in the case of friction factor and Nusselt Number but the variation of Reynolds Number strongly affects the Nusselt Number as compared the friction factor.

Optimization plot of the solar air heater

The optimization plot has been draw to determine the optimum values of input variables to achieve the maximum Nusselt Number, maximum TPF and minimum friction factor. The effectiveness of the optimization plot has been determined by the desirability and the composite desirability of the responses. It represents the closeness of the response variables with its ideal values within the range of the 0–1. The best and worst values of the desirability is 0 and 1. The overall desirability of the optimization is 0.9424 as representing Figure 25 that is very close to 1 shows the best correlation of the responses with input variables. The desirability of the TPF, friction factor and Nusselt Number is 1, 0.83685 and 1 which shows that TPF and Nusselts Number shows the best correlation of responses with input variables within the range. The optimum values of the Reynolds Number and P/L are 16,928.2180 and 1.3430. The maximum values of the responses TPF and Nusselt Number are 1.8903 and 176.5064 and minimum value of friction factor is 0.0260.

Validation of the results

After finding the optimum geometry of the SAH, the experimental setup has been developed and with the help of experimental data repose parameters calculate. The experimental results has been further validated with predicted values of the responses. Table 14 represented the experimental and predicted results.

Pressure drop in SAH

Figure 26 represents the pressure drop at the surface of SAH at different Reynolds number. Figure 26 clearly shows that if the Reynolds number increases then the friction factor increases due to increase of mass flow rate of air. The fin geometry is represented by the pitch to the height ratio of the fins. If the P/L ratio increases then the pressure drop is increased since more obstruction is provided by the fins.⁵¹

Validation of CFD results with experimental results

In this section, the outlet temperature of the air, thermal efficiency, and exergy of the SAH has been determined numerically and experimentally and validated. Figure 27(a) represents the outlet temperature of air from 9 am to 6 pm. Figure 27(a) clearly shows that the outlet temperature of air increases from 9 am to 12 pm and then starts to reduce since the outlet temperature of outlet air is very much dependent on solar flux. As solar flux increases from 9 am to 12 pm and then solar flux continuously reduces. The numerical

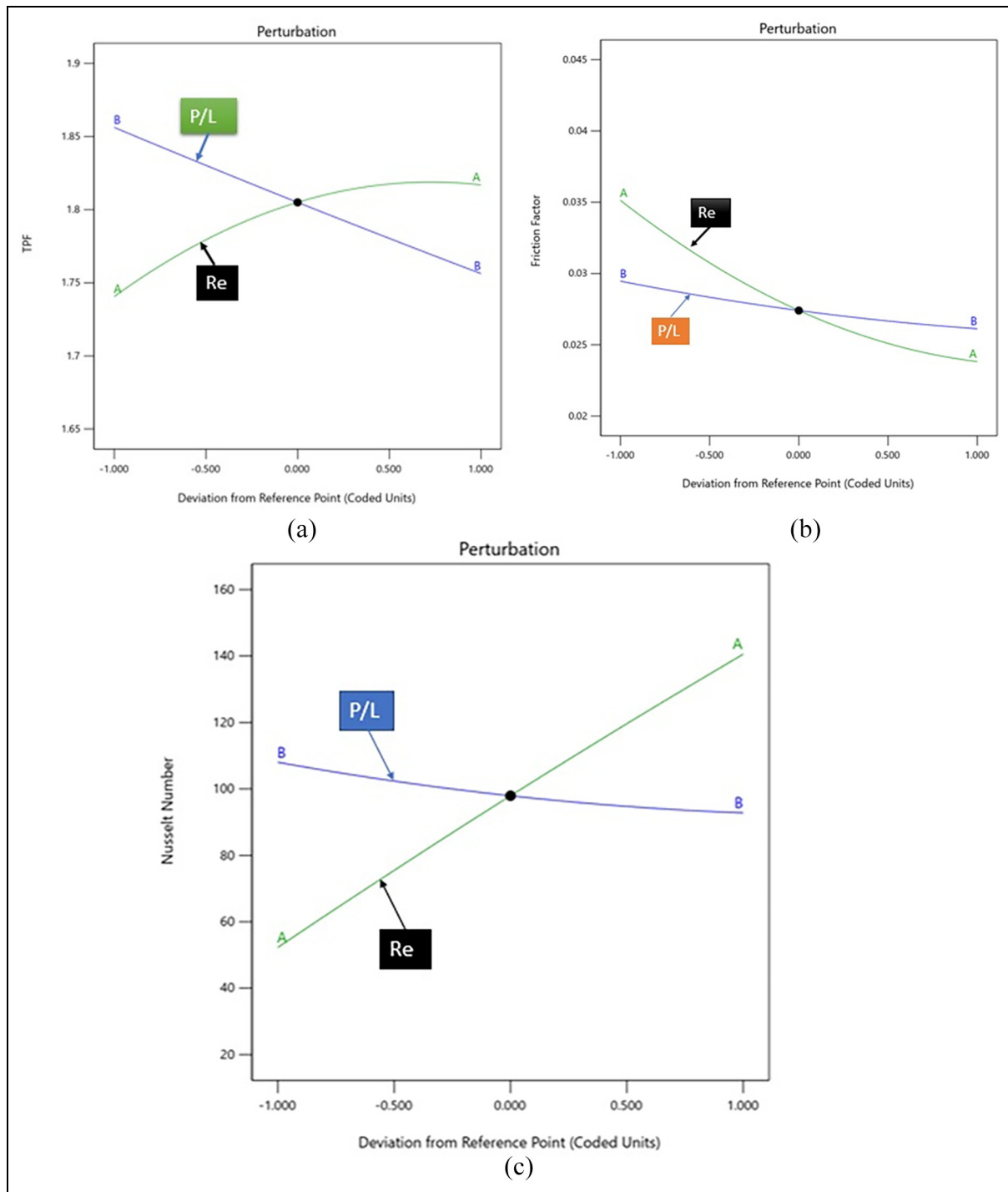


Figure 24. Perturbation of the responses with input variables: (a) TPF with input variables, (b) friction factor with input variables, and (c) Nusselt Number variation input variables.

Table 14. Validation of experimental and predicted results.

Responses	Nu	f	TPF
Experimental results	176.5064	0.0260	1.8903
Predicted results	181.21	0.02689	1.9624
% Error	2.6	3.42	3.82

and experimental results of outlet temperature of air is validated with accuracy of 3%–4%.

Figure 27(b) represents the thermal efficiency of solar air heater. Figure 27(b) shows the maximum efficiency of SAH is near to 70% and the results of CFD finding are validated with accuracy of 4%–6% with experimental results. Figure 28 shows the exergy

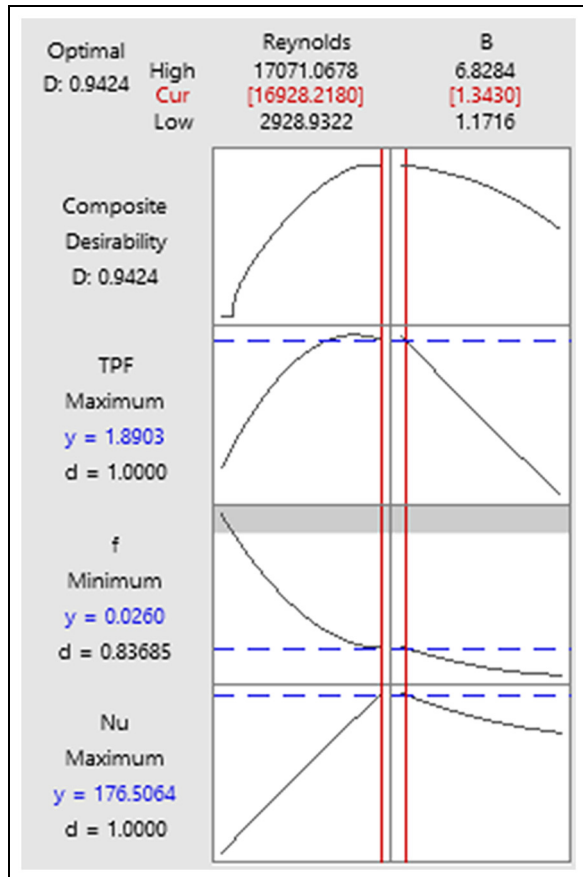


Figure 25. Optimization plots of responses.

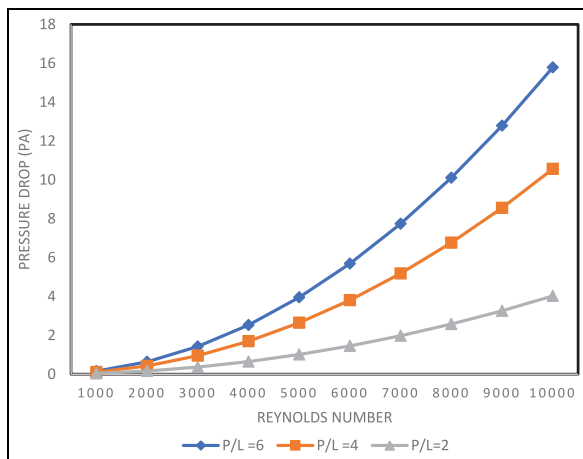


Figure 26. Pressure drop with Reynolds number at different fin geometry.

variation with the time of the day. The exergetic efficiency of the SAH depends on the mass flow rate, solar flux and gain in outlet temperature of air. So as the solar flux increase the gain in exergy is also increases which increase the exergetic efficiency. The maximum exergy efficiency of the SAH has to be recorded to be 6.5% and CFD and experimental results are validated with 4%–5% accuracy. The

exergy efficiency of solar air heater is quite lesser than the thermal efficiency due to lot of turbulence and irreversibility are presents inside the solar air heater which reduces the exergy efficiency of solar air heater.

Conclusion

This paper investigates the flow field of finned SAH by CFD and Experimental analysis. The main work targeted to optimize the geometry of fins for maximize the heat transfer rate and minimize the blower pressure drops. For optimization purpose RSM tool is used. The RSM generate the performance parameters in the form of second order polynomial. The input variables selected to be Reynolds number and the fins pitch length ratio. The following points have been concluded as the final outcomes of this research.

1. The fin pitch to height or length ratio play the important role in HT and pressure drop. If the P/L ratio increases then the friction factor and heat transfer coefficient both reduces. The optimum value of the P/L is 1.3430 at which Nusselt Number is 176.50 and friction factor is 0.026.
2. The higher value of the Reynolds Number shows the higher turbulence in the SAH. So if Reynolds Number increases then the friction factor is decreases and the heat transfer coefficient increases. The optimum value of Reynolds number found to be 16,928.
3. The Thermal Performance Factor (TPF) is the important factor which measure the enhancement of the Nusselt Number as compared to friction factor on finned surface reference to the smooth surface. The optimum value of the TPF is obtained to be 1.8903, shows the use of fins is beneficial for the SAH.
4. The fins increases the heat transfer and Nusselt Number but simultaneously enhance the pressure drop and blower power.
5. The maximum thermal and exergy efficiency of SAH found to be 74% and 6.5% respectively.
6. The maximum outlet temperature of solar air heater by Numerical and experimental study were found to be 94°C and 92°C respectively.
7. The second order non-linear model generated by the ANOVA analyses is significant since the value of the p is less than 0.0001.
8. The ANOVA analysis represents the composite desirability of the optimization plots to be 0.9424 which shows the best correlation among input and output variables.
9. The ANOVA analyses shows that the adjusted R^2 and Predicted R^2 values for Nusselt Number, Friction factor and TPF are namely 0.9995 and 0.9981, 0.9846 and 0.9363, and 0.9533 and 0.8243, respectively.

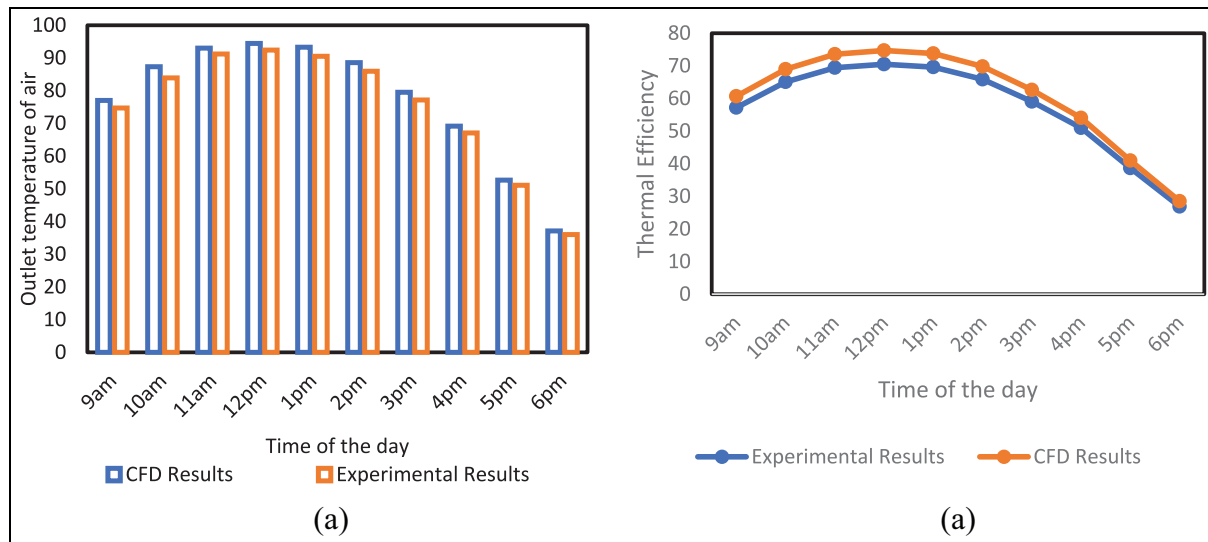


Figure 27. Outlet temperature and the thermal efficiency of SAH: (a) outlet temperature variation through out the day and (b) thermal efficiency of SAH.

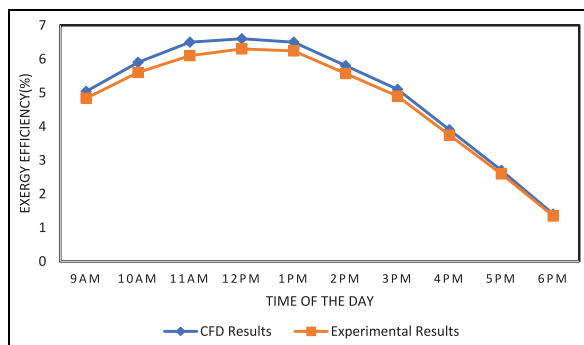


Figure 28. Exergy efficiency of SAH.

10. The perturbation plots shows that, the Nusselt Number and friction factor are strongly depends on the Reynolds Number as compared to P/L ratio due to sharp curvature of the Reynolds Number curve.
11. The Nusselt Number, Friction Factor and TPF optimization predicted results are validated with experimental results of the accuracy of the 2.6%, 3.42%, and 3.82%.


Declaration of conflicting interests

The author declared no potential conflicts of interest with respect to the research, authorship, and/or publication of this article.

Funding

The author received no financial support for the research, authorship, and/or publication of this article.

ORCID iD

Vineet Singh  <https://orcid.org/0000-0003-3328-2588>

References

1. Sahu MK and Prasad RK. Exergy based performance evaluation of solar air heater with arc-shaped wire roughened absorber plate. *Renew Energy* 2016; 96: 233–243.
2. Sahu MK, Kharub M and Matheswaran MM. Nusselt number and friction factor correlation development for arc-shape apex upstream artificial roughness in solar air heater. *Environ Sci Pollut Res* 2022; 29(43): 65025–65042.
3. Elmasry Y, Chaturvedi R, Ali A, et al. Numerical analysis and RSM modeling of the effect of using a V-cut twisted tape turbulator in the absorber tube of a photo-voltaic/thermal system on the energy and exergy performances of the system. *Eng Anal Bound Elem* 2023; 155: 340–350.
4. Xiao H, Wang J, Liu Z, et al. Turbulent heat transfer optimization for solar air heater with variation method based on exergy destruction minimization principle. *Int J Heat Mass Transf* 2019; 136: 1096–1105.
5. Bauri SK and Prasad AK. A CFD-based thermal analysis of solar air heater duct artificially roughened with ‘S’ shape ribs on absorber plate. *AIP Conf Proc* 2021; 2341(1): 030009.
6. Mahanand Y and Senapati JR. Thermo-hydraulic performance analysis of a solar air heater (SAH) with quarter-circular ribs on the absorber plate: A comparative study. *Int J Therm Sci* 2021; 161: 1–23. DOI: 10.1016/J.IJTHEMALSCI.2020.106747
7. Gill RS, Hans VS and Singh RP. Optimization of artificial roughness parameters in a solar air heater duct roughened with hybrid ribs. *Appl Therm Eng* 2021; 191: 1–12.
8. Sahu MK, Sharma M, Matheswaran MM, et al. On the use of longitudinal fins to enhance the performance in rectangular duct of solar air heaters—a review. *J Sol Energy Eng* 2019; 141(3): 1–44. DOI: 10.1115/1.4042827
9. Fudholi A, Sopian K, Ruslan MH, et al. Performance and cost benefits analysis of double-pass solar collector

- with and without fins. *Energy Convers Manag* 2013; 76: 8–19.
10. Borah PP, Pathak KK, Gupta A, et al. Experimental study of a solar air heater with modified absorber plate through square obstacles with threaded pin fins. *Appl Therm Eng* 2023; 228: 1https://innovationspace.ansys.com/knowledge/forums/topic/skewness-in-ansys-meshing-2/18.
 11. Sivakumar S, Siva K and Mohanraj M. Experimental thermodynamic analysis of a forced convection solar air heater using absorber plate with pin-fins. *J Therm Anal Calorim* 2019; 136(1): 39–47.
 12. Akhbari M, Rahimi A and Hatamipour MS. Modeling and experimental study of a triangular channel solar air heater. *Appl Therm Eng* 2019; 170: 1https://innovation space.ansys.com/knowledge/forums/topic/skewness-in-ansys-meshing-2/15.
 13. Du J, Chen H, Li Q, et al. Turbulent flow-thermal-thermodynamic characteristics of a solar air heater with spiral fins. *Int J Heat Mass Transf* 2024; 226: 1https://innovationspace.ansys.com/knowledge/forums/topic/skewness-in-ansys-meshing-2/16.
 14. Alsaiani AO, Alzahrani HAH N M, et al. Heat transfer augmentation in a solar air heater with conical roughness elements on the absorber. *Case Stud Therm Eng* 2022; 36: 1https://innovationspace.ansys.com/knowledge/forums/topic/skewness-in-ansys-meshing-2/14.
 15. Miao L, Wan R, Wu HW, et al. Heat transfer and pressure drop characteristic research of sine wavy flying-wing fins. *Sci Rep* 2023; 13(1): 1–14.
 16. Ammar M, Mokni A, Mhiri H, et al. Numerical analysis of solar air collector provided with rows of rectangular fins. *Energy Rep* 2020; 6: 3412–3424.
 17. Sharma S and Maithani R. A computational study on thermal and sustainability analysis of solar air heater with S and airfoil tabulators. *Evergr* 2024; 11(1): 295–305.
 18. Nagaraj M, Reddy MK, Honnesara Sheshadri AK, et al. Numerical analysis of an aerofoil fin integrated double pass solar air heater for thermal performance enhancement. *Sustainability* 2022; 15(1): 591.
 19. Yadav AS, Shrivastava V, Sharma A, et al. Numerical simulation and CFD-based correlations for artificially roughened solar air heater. *Mater Today Proc* 2021; 47: 2685–2693.
 20. Gogada S, Roy S, Gupta A, et al. Energy and exergy analysis of solar air heater with trapezoidal ribs based absorber: A comparative analysis. *Energy Sci Eng* 2023; 11(2): 585–605.
 21. Yadav AS and Bhagoria JL. A CFD (computational fluid dynamics) based heat transfer and fluid flow analysis of a solar air heater provided with circular transverse wire rib roughness on the absorber plate. *Energy* 2013; 55: 1127–1142.
 22. Singh AP and Singh OP. Performance enhancement of a curved solar air heater using CFD. *Sol Energy* 2018; 174: 556–569.
 23. Gawande VB, Dhoble AS, Zodpe DB, et al. Experimental and CFD investigation of convection heat transfer in solar air heater with reverse L-shaped ribs. *Sol Energy* 2016; 131: 275–295.
 24. Sun W, Ji J and He W. Influence of channel depth on the performance of solar air heaters. *Energy* 2010; 35(10): 4201–4207.
 25. Al-Damook M, Obaid ZAH, Al Qubeissi M, et al. Cfd modeling and performance evaluation of multipass solar air heaters. *Numer Heat Transf A Appl* 2019; 76(6): 438–464.
 26. Parsa H, Saffar-Avval M and Hajmohammadi MR. 3d simulation and parametric optimization of a solar air heater with a novel staggered cuboid baffles. *Int J Mech Sci* 2021; 205: 1https://innovationspace.ansys.com/knowledge/forums/topic/skewness-in-ansys-meshing-2/16.
 27. Qader BS, Supeni EE, Ariffin MKA, et al. RSM approach for modeling and optimization of designing parameters for inclined fins of solar air heater. *Renew Energy* 2019; 136: 48–68.
 28. Srivastava A, Chhaparwal GK and Sharma RK. Numerical and experimental investigation of different rib roughness in a solar air heater. *Therm Sci Eng Prog* 2020; 19: 1https://innovationspace.ansys.com/knowledge/forums/topic/skewness-in-ansys-meshing-2/12.
 29. Garg GDHP, Ranjana J and Choudhury C. Theoretical analysis on a new finned type solar air heater. *Angew Chem Int Ed* 1967; 6(11): 951–952, , pp. 5–24.
 30. Karim M and Hawlader M. Performance investigation of flat plate, v-corrugated and finned air collectors. *Energy* 2006; 31(4): 452–470.
 31. El-Sebaei AA, Aboul-Enein S, Ramadan MRI, et al. Thermal performance investigation of double pass-finned plate solar air heater. *Appl Energy* 2011; 88(5): 1727–1739.
 32. Velmurugan P and Kalaivanan R. Energy and exergy analysis of solar air heaters with varied geometries. *Arab J Sci Eng* 2015; 40(4): 1173–1186.
 33. Naphon P. On the performance and entropy generation of the double-pass solar air heater with longitudinal fins. *Renew Energy* 2005; 30(9): 1345–1357.
 34. Bahrehmand D, Ameri M and Gholampour M. Energy and exergy analysis of different solar air collector systems with forced convection. *Renew Energy* 2015; 83: 1119–1130.
 35. Priyam A and Chand P. Thermal and thermohydraulic performance of wavy finned absorber solar air heater. *Sol Energy* 2016; 130: 250–259.
 36. Matheswaran MM, Arjunan TV, Muthusamy S, et al. A case study on thermo-hydraulic performance of jet plate solar air heater using response surface methodology. *Case Stud Therm Eng* 2022; 34: 1https://innovationspace.ansys.com/knowledge/forums/topic/skewness-in-ansys-meshing-2/14. DOI: 10.1016/J.CSITE.20 22.10 1983
 37. ANSYS FLUENT 12.0 Theory Guide - 5.3.4 Rosse-land Radiation Model Theory, <https://www.afs.enea.it/project/neptunius/docs/fluent/html/th/node113.htm> (accessed 14 August 2022).
 38. ANSYS FLUENT 12.0 Theory Guide - 5.3.3 P-1 Radiation Model Theory, <https://www.afs.enea.it/project/neptunius/docs/fluent/html/th/node112.htm#eq-p1-gamma> (accessed 14 August 2022).
 39. Daabo AM, Al-Mola YS, Al-Rawy AY, et al. State of the art single-objective optimization of small scale cylindrical cavity receiver. *Sustain Energy Technol Assess* 2019; 35: 278–290.
 40. Skewness in ANSYS meshing - illustrated explanation, <https://innovationspace.ansys.com/knowledge/forums/topic/skewness-in-ansys-meshing-2/> (accessed 14 August 2022).

41. Aghakhani S and Afrand M. Experimental study of the effect of simultaneous application of the air- and water-cooled flow on efficiency in a photovoltaic thermal solar collector with porous plates. *Appl Therm Eng* 2022; 217: 1–11.
42. Singh V, Yadav VS, Barnawi AB, et al. Comparison of different designs of solar air heater with the simple solar heater of having reflecting mirrors. *Proc IMechE, Part C: J Mechanical Engineering Science* 2023; 237(21): 5156–5173.
43. Singh V and Yadav VS. Optimizing the performance of solar panel cooling apparatus by application of response surface methodology. *Proc IMechE, Part C: J Mechanical Engineering Science* 2022; 236(22): 11094–11120.
44. Kumar R, Goel V, Singh P, et al. Performance evaluation and optimization of solar assisted air heater with discrete multiple arc shaped ribs. *J Energy Storage* 2019; 26: 1–17. DOI: 10.1016/J.EST.2019.100978
45. Singh V and Yadav VS. Application of RSM to optimize solar pump LCOE and power output. *IETE J Res* 2023; 69(11): 8226–8237.
46. Singh V, Kumar M, Kumar N, et al. Optimization and validation of solar pump Performance by MATLAB Simulink and RSM. *Evergr* 2022; 9(4): 1110–1125.
47. Liu X, Gui N, Wu H, et al. Numerical simulation of flow past a triangular prism with fluid–structure interaction. *Eng Appl Comput Fluid Mech* 2020; 14(1): 462–476.
48. Zulkifli I, Alwaeli AHA, Ruslan MH, et al. Numerical investigation of V-groove air-collector performance with changing cover in Bangi, Malaysia. *Case Stud Therm Eng* 2018; 12: 587–599.
49. Kumar A and Layek A. Thermo-hydraulic performance of roughened solar air heater by design of experiment and meta-heuristic approach. *Therm Sci Eng Prog* 2019; 10: 92–102.
50. Daabo AM, Mahmoud S and Al-Dadah RK. The effect of receiver geometry on the optical performance of a small-scale solar cavity receiver for parabolic dish applications. *Energy* 2016; 114: 513–525.
51. Singh I and Vardhan S. Experimental investigation of an evacuated tube collector solar air heater with helical inserts. *Renew Energy* 2021; 163: 1963–1972.
52. Aghakhani S, Afrand M, Karimipour A, et al. Numerical and experimental study of thermal efficiency of a spiral flat plate solar collector by changing the spiral diameter, flow rate, and pipe diameter. *Sustain Energy Technol Assess* 2022; 53: 1–14.
53. Singh and S. Vardhan. Experimental investigation of an evacuated tube collector solar air heater with helical inserts. *Renew Energy* 2021; 163: 1963–1972, Jan. 2021.

Appendix

Notation

C_p	Specific heat of air. (W/m ² K).
h_r	Radiation heat transfer coefficient. (W/Km ²).
N_{uL}	Nusselt number.
R_{aL}	Rayleigh number.
θ	Tilt angle.
E_{XIN}	Exergy entering in the solar air heater.
E_{XOUT}	Exergy leak in the atmosphere.
E_{XDEST}	Exergy destruction due to irreversibility in the system.
hc	Heat transfer coefficient W/m ² K.
T_p	AP temperature (K).
T_a	Atmospheric temperature (K).
S_F	Solar Flux (W/m ²).
T_{Sun}	Sun temperature (K).
V	Velocity of air flow over the SAH cover plate (m/s).
T_{sky}	Sky temperature(K).
y	Inaccuracy in measurement.

Symbols

ρ	Density of Air (Kg/m ³).
σ	Stefan Boltz's man constant (5.67×10^{-8})
ϵ	Emissivity of solar panel material.
k	Boltzmann constant.
α	Absorptivity or Absorption Coefficient.
η	Efficiency of fin
η_{SAH}	Efficiency of Solar Air Heater
Ψ	Exergetic efficiency of SAH

Acronyms

SAH	Solar Air Heater
SSAH	Simple Solar Air Heater
SSAHF	Simple Solar Air Heater with Fins
PD	Pressure Drop
HT	Heat Transfer
HTC	Heat Transfer Coefficient
AP	Absorber Plate
PCM	Phase Change material
RN	Reynolds Number
MFR	Mass Flow rate
CFD	Computational Fluid Dynamics
RSM	Response Surface Methodology
FF	Friction Factor